DOCTORAL DISSERTATION

Magnetic and thermal properties of caged cubic compounds RT_2Al_{20} (R = Nd, Tm and T = Ti, V)

かご状立方晶化合物 RT_2Al_{20} (R = Nd, Tm, T = Ti, V)の磁気的および熱的物性

Qiankun Lei

Supervisor: Prof. Katsuhiko Nishimura

Graduate School of Science and Engineering for Education

University of Toyama

Toyama, Japan

July, 2016

Abstract

The ternary intermetallic compounds RT_2X_{20} (R = rare earths and uranium, T = transition metals, X = Al, Zn and Cd) crystallize in the cubic $CeCr_2Al_{20}$-type structure (space group: $Fd\bar{3}m$, No. 227), where R ions are encapsulated in the Frank-Kasper cages formed by sixteen neighboring X ions. The magnetic properties of most rare earth compounds RT_2X_{20} are determined by the rare-earth magnetic moments that origin in the partially filled 4*f* electronic shell. Due to the unique crystal structure of RT_2X_{20}, localized 4*f* electrons of R ions can obtain itinerancy by hybridizing with conduction electrons in *s*, *p*, and *d* shells. Because of the competing localized and itinerant characters of the 4*f* electrons, some of the caged compounds of RT_2X_{20} manifest a diverse range of novel physical properties at low temperatures, such as heavy fermion behavior, valence fluctuations, multipole ordering, quantum criticality, and unconventional superconductivity. The studies of these attractive physical properties will lead to deeper understandings of the basic problems of physics as well as potential spintronic and thermoelectric applications.

In the RT_2X_{20} system, magnetic properties of RT_2Zn_{20} (R = rare earth, T = Fe, Co, Ru, Rh, Os, and Ir) have been systematically investigated, and a wide variety of correlated electron phenomena have been observed. The isostructural compounds RT_2Al_{20} (R = rare earth, T = Ti, V, Cr, Mn, Nb, Mo, Ta, and W) are expected to have similar intriguing physical properties, which have been reported for PrT_2Al_{20} (T = Ti, V, Cr, and Nb), SmT_2Al_{20} (T = Ti, V, Cr, and Ta), $TmTi_2Al_{20}$, and YbT_2Al_{20} (T = Ti, V and Cr).

In this thesis, we focus on the Nd-based compounds NdT_2Al_{20} (T = Ti, V) with Kramers $4f^3$ configurations of Nd^{3+} ions and the Tm-based system TmV_2Al_{20} with non-Kramers $4f^{12}$ configurations of Tm^{3+} ions, where Nd and Tm are neighboring elements of Pr and Yb, respectively, and Tm^{3+} ($4f^{12}$) ion is the hole analog of Pr^{3+} ($4f^2$) ion. Single crystals of the RT_2Al_{20} (R = Nd, Tm and T = Ti, V) as well as the nonmagnetic isostructural single crystals of RT_2Al_{20} (R = La, Lu and T = Ti, V) were made by the Al-self flux method. The crystal structures were determined by powder X-ray diffraction. The crystallographic orientations of the selected single crystals were obtained by Laue back-reflection of X-rays, and the oriented single crystals were cut along required directions by a spark erosion cutting machine for further anisotropic measurements. Magnetic and transport properties of single crystalline RT_2Al_{20} (R = Nd, Tm and T = Ti, V) were investigated systematically with the nonmagnetic reference compounds RT_2Al_{20} (R = La, Lu and T = Ti, V).

An antiferromagnetic (AFM) phase transition was observed in $NdTi_2Al_{20}$ at T_N = 1.4 K. The temperature dependence of magnetization follows the Curie-Weiss law above 100 K in an applied field of 0.1 T along the [110] direction, with an effective magnetic moment μ_{eff} = 3.56 μ_B (Nd^{3+}: 3.64 μ_B) and a Curie-Weiss temperature θ_P = − 28.50 K. Specific heats of the $NdTi_2Al_{20}$ and $LaTi_2Al_{20}$ single crystals were measured in applied fields up to 9 T. Magnetic specific heats of $NdTi_2Al_{20}$ were obtained by subtracting the experimental data of single crystalline $LaTi_2Al_{20}$ from those of $NdTi_2Al_{20}$ single crystals. No observable anisotropy was found in magnetization or specific heat measurements in small applied fields at low temperatures. A noticeable change of slope in magnetic entropy S_{mag} (T) was observed near 5 K in zero field where S_{mag} (T) = R ln 2 [5.76 J/mol·K, R is the gas constant]. These results

suggest a Γ_6 doublet ground state of the Nd^{3+} ion in $NdTi_2Al_{20}$. The experimental results were analyzed by theoretical calculations, and a CEF scheme Γ_6 (0 K, doublet) – $\Gamma_8^{(1)}$ (53K, quartet) – $\Gamma_8^{(2)}$ (443 K, quartet) was proposed.

The magnetization M and specific heat C were measured for single crystals of NdV_2Al_{20} in the temperature range from 0.5 to 300 K with applied magnetic fields along the three principal axes, [100], [110], and [111]. Temperature dependences of resistivities for NdV_2Al_{20} and the LaV_2Al_{20} were measured down to 1.9 K in zero field. A ferromagnetic (FM) phase transition was observed at the Curie temperature $T_C = 1.8$ K in both magnetization and specific heat measurements. The field dependences of M show an anisotropy at 0.5 K. The easy axis of magnetization is [100] at low fields and changes to [110] in applied fields above 2 T. On cooling below 2 K in zero field, the specific heat divided by temperature C/T shows an enhanced value with a large electronic specific heat coefficient γ of about 2 J/(mol·K^2). A large C / T value of more than 1 J/(mol·K^2) remains in an applied field of 9 T below T_C. The magnetic entropy S_{mag} for NdV_2Al_{20} in zero field is R ln 4 near the Curie temperature T_C and reaches R ln 6 near 20 K, suggesting a quartet ground state and a doublet first excited state. The temperature dependence of resistivity for NdV_2Al_{20} shows a $-\log T$ dependence around 10 K. The CEF calculations for energy scheme were carried out, which were found to be unable to explain the observed magnetizations and specific heats consistently. These results suggest a heavy fermion state for NdV_2Al_{20}.

Physical properties of TmV_2Al_{20} single crystals were investigated by magnetization, specific heat, and electrical resistivity measurements. No phase transition has been observed

down to 0.5 K. Magnetic anisotropy measurements clarified the easy and hard axes of magnetization are along the [100] direction and [111] direction, respectively. The specific heat of nonmagnetic isostructural single crystal of LuV_2Al_{20} was used to obtain the magnetic specific heats of the TmV_2Al_{20}. The C_{mag} / T value increases up to 6 J/(mol·K^2) near 0.6 K when cooled down below 2 K in zero external field. The magnetic entropy in zero field reaches R ln 5 near 10 K, suggesting that the ground state of Tm^{3+} ions is a nonmagnetic doublet state with the first excited magnetic triplet state nearby (a pseudo-fivefold degenerate state). The electrical resistivity for TmV_2Al_{20} was measured down to 2 K, an overall CEF splitting of about 90 K was suggested by the observed magnetic part of resistivity. The experimental results were reproduced by theoretical calculations, and an energy level scheme was proposed: Γ_3 (0 K, doublet) – $\Gamma_5^{(1)}$ (2 K, triplet) – Γ_2 (59 K, singlet) – $\Gamma_5^{(2)}$ (65 K, triplet) – Γ_4 (74 K, triplet) – Γ_1 (85 K, singlet). The enhanced value of C_{mag} / T in the lowest temperature region in zero field was explained by assuming an energy splitting of the doublet ground state.

Table of contents

Abstract ..... **I**

Table of contents ..... **V**

1. Introduction **1**

1.1. Rare earth intermetallic compounds 1

1.2. Cubic crystal structure of RT_2X_{20} 1

1.3. Review of previous studies on RT_2X_{20} 3

1.4. Outline of the thesis 6

2. Theoretical background **8**

2.1. Localized magnetism of rare earths 8

2.1.1. Hund's rules 10

2.1.2. Curie law and Curie-Weiss law 12

2.1.3. Kondo effect and RKKY interaction 15

2.2. Crystalline electric field effects 17

2.2.1. Stevens equivalent operators 18

2.2.2. Crystalline electric field in cubic symmetry 19

3. Experimental methods **22**

3.1. Sample preparation 22

3.1.1. Growth of single crystal 22

3.1.2. Powder X-ray diffraction 25

3.1.3. Single crystal orientation 27

3.2. Measurements of physical properties 28

3.2.1. Magnetization measurement 28

3.2.2. Specific heat measurement 29

3.2.3. Electrical resistivity measurement 29

4. Antiferromagnetic ordering in $NdTi_2Al_{20}$ single crystals 30

4.1. Experimental results 30

4.1.1. Magnetic properties 30

4.1.2. Specific heat and magnetic entropy 33

4.1.3. Electrical resistivity 37

4.2. Analyses and discussion 38

4.3. Conclusion 43

5. Possible heavy fermion state of the caged cubic compound NdV_2Al_{20} 45

5.1. Experimental results 45

5.1.1. Magnetic properties 45

5.1.2. Specific heat and magnetic entropy 48

5.1.3. Electrical resistivity 51

5.2. Analyses and discussion 52

5.3. Conclusion 54

6. Magnetic and thermal properties of TmV_2Al_{20} 56

6.1. Experimental results 56

6.1.1. Magnetic properties 56

6.1.2. Specific heat and magnetic entropy 58

6.1.3. Electrical resistivity 60

6.2. Analyses and discussion 61

6.3. Conclusion 67

References 68

List of publications 80

List of tables 82

List of figures 83

Acknowledgements 89

1. Introduction

1.1. Rare earth intermetallic compounds

In the past few decades, intermetallic compounds containing rare earths and / or transition metals have been intensively investigated for their structures and versatile physical properties, such as RT_2X_{20} (R = rare earths and U, T = transition metals, X = Al, Zn, and Cd) [1–10], RT_2Al_{10} (R = rare earths, T = transition metals) [11–18], filled skutterudites RT_4X_{12} (R = rare earths and U, T = Fe, Ru, Os, X = P, As, Sb) [19–27], and RTX (R = rare earths, T = transition metals, X = p-block elements) [28–34]. These rare-earth-based intermetallic compounds provide rich testing grounds for studying the magnetic properties associated with the 4f electrons in both local moment and correlated electron systems. A wide variety of interesting physical phenomena like Kondo effect [35,36], heavy fermion behavior [3,5,37–42], mixed valences [43–46], multipole ordering [47–49], quantum criticality [44,50–52], and unconventional superconductivity [53,54] have been observed in these compounds.

1.2. Cubic crystal structure of RT_2X_{20}

The ternary intermetallic compounds RT_2X_{20} crystallize in the cubic $CeCr_2Al_{20}$-type structure (space group: $Fd\bar{3}m$, No. 227). [55–58] The crystal structure is shown in Figure 1.1, in which R (8a) and T (16d) atoms each occupy their single unique sites with cubic (T_d) and trigonal ($\bar{3}m$) point symmetry respectively, and X atoms have three different sites, i.e., 16c, 48f, and 96g for X(1), X(2), and X(3), respectively [1,10,59–62]. Since R and T atoms

are exclusively encapsulated in the Frank-Kasper polyhedron formed by *X* atoms, there are no *R*–*R*, *T*–*T* or *R*–*T* nearest neighbors (NN) and rare-earth magnetic moments are well isolated from each other. On the other hand, *R* atoms are surrounded by sixteen *X* atoms with large coordination number, which will lead to strong hybridization between the surrounding conduction electrons and the 4*f* electrons (*c*-*f* hybridization) despite of the well-localized character of the 4*f* electrons. [8,63–65] The unique crystal structure and electronic structures bring about various exciting physical phenomena and provide an opportunity to study the strongly correlated electronic states.

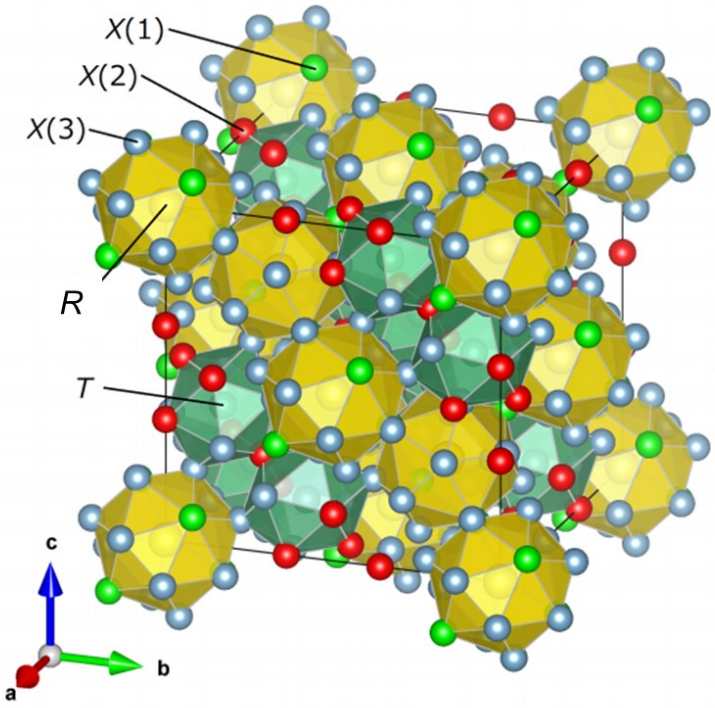

Figure 1.1: Crystal structure of RT_2X_{20}. *R* (8*a*) and *T* (16*d*) atoms each occupy their single unique sites with cubic (T_d) and trigonal ($\bar{3}m$) point symmetry respectively, and *X* atoms have three different sites, i.e., 16*c*, 48*f*, and 96*g* for *X*(1) , *X*(2) , and *X*(3) , respectively. [65]

1.3. Review of previous studies on RT_2X_{20}

The ternary intermetallic caged compounds RT_2X_{20} (R = rare earths and U, T = transition metals, X = Al, Zn, and Cd) have been studied intensively experimentally and theoretically due to their unique structure and novel physical properties, especially when the 4*f* or 5*f* shell of R ion is close to empty, full or half filled (Ce, Pr, Sm, Yb, and U). [2,5,9,66,67]

In these compounds, R ion locates in a cubic symmetry site (T_d) surrounded by a cage of sixteen X ions as its nearest neighbors. Because of the large coordination number, strong hybridizations between the conduction electrons (*c* electrons) and the 4*f* electrons of the rare earth ions are expected. [68,69] The *c-f* hybridization may result in a large density of states (DOS) near the fermi surface and various correlated electron behaviors.

Ce-based compound $CeRu_2Zn_{20}$ is found to be a dense Kondo compound, and shows typical behaviors of a heavy fermion system with enhanced magnetic susceptibility and electronic specific-heat coefficient due to a large density of states at the fermi energy. [9]

Pr-based compounds PrT_2Zn_{20} (T = Ir, Rh) [47,54,70–73] and PrT_2Al_{20} (T = Ti, V, Cr, Nb) [2,3,36,37,48,53,65,74–84] have been intensively investigated because of their correlated electron behaviors, such as Kondo effects, multipolar order, and heavy fermion superconductivity. In most of the Pr-based 1-2-20 systems, the CEF ground state is a non-Kramers doublet Γ_3 state without magnetic dipole moment. A degenerate ground state with multipoles and multipole ordering can be realized in the cubic CEF.

Quadrupole ordering at T_Q = 0.11 K and superconducting state below T_C = 0.05 K have been found in $PrIr_2Zn_{20}$. [47] Simultaneous superconducting and AFM transitions occur at $T_C = T_Q$ = 0.06 K in $PrRh_2Zn_{20}$, in which the Pr^{3+} is the non-Kramers Γ_3 doublet with the quadrupolar degrees of freedom. [72] PrT_2Al_{20} (T = Ti, V) with the non-Kramers doublet Γ_3 ground state show Kondo effects and multipole ordering. Chemical pressure effect induced by the smaller ionic radius of V than Ti leads to stronger Kondo coupling, enhanced Kondo effect, and the suppression of the quadrupolar ordering in PrV_2Al_{20}, compared to $PrTi_2Al_{20}$. [36,53,76,79,82] $PrTi_2Al_{20}$ and PrV_2Al_{20} exhibit FM and AFM quadrupolar phase transitions at T_{FQ} = 2 K and T_{AFQ} = 0.6 K, respectively. [36,48,78] Superconductivity was found at T_C = 200 mK in $PrTi_2Al_{20}$ with the nonmagnetic ferroquadrupolar state. The quadrupolar Kondo lattice $PrTi_2Al_{20}$ exhibits superconductivity at T_C = 200 mK in the nonmagnetic ferroquadrupolar state. [53] Superconductivity at T_C = 50 mK in the antiferroquadrupole-ordered state and double transitions at T_Q = 0.75 K and T^* = 0.65 K associated with quadrupole and octupole degrees of freedom of the Γ_3 doublet were observed in PrV_2Al_{20}. [82]

$PrCr_2Al_{20}$ was found to be Kondo lattice and no phase transition was observed down to 400 mK in electrical resistivity measurement or 1.8 K in magnetic susceptibility measurements. [59] No phase transitions has been found down to 0.6 K in $PrNb_2Al_{20}$ in magnetization, electrical resistivity and specific heat measurements. A non-Kramers Γ_3 doublet ground state was proposed, and a upturn in C/T and a non-Fermi liquid behavior in resistivity at low temperatures were observed. [69] The ^{93}Nb nuclear quadrupole resonance

(NQR) demonstrated the absence of magnetic dipole phase transition down to 75 mK in $PrNb_2Al_{20}$. [75]

Unusual field-insensitive phase transitions, heavy fermion behaviors, and mixed valence states have been found in Sm-based compounds SmT_2Al_{20} (T = Ti, V, Cr, and Ta) [35,66,85]

Yb-based compounds YbT_2Zn_{20} (T = Fe, Co, Ru, Rh, Os, and Ir) are heavy electron compounds with large local moment degeneracy. [5,86] A field-induced antiferro-quadrupolar ordering based on the Γ_3-type quadrupole moment has been reported for the heavy fermion compound $YbCo_2Zn_{20}$. [87]

Some of the U-based compounds heavy fermion compounds have also been reported, such as localized heavy fermion compounds UM_2Zn_{20} (M = Co, Rh) [88], and heavy fermion compound UIr_2Zn_{20} with a paramagnetic ground state. [89]

However, the other rare earths systems in the RT_2X_{20} family which are expected to manifest similar interesting physical properties have rarely been studied [90]. As hole analogs of PrT_2X_{20} (Pr^{3+}: $4f^2$), the Tm-based compounds TmT_2X_{20} (Tm^{3+}: $4f^{12}$), which might be of similar attractive physical properties, are of particular interest to us.

Although no strongly correlated electronic system has been discovered in NdT_2X_{20} system. Interesting phenomena have been reported for some of the Nd-based intermetallic compounds. Quadrupolar susceptibility [91], unusual local disorder [19], as well as ferromagnetism and possible heavy-fermion behavior [92] have been observed in single crystals of filled-skutterudite $NdOs_4Sb_{12}$, which also crystalizes in cubic structure (space

group: $Im\overline{3}$, No.204). $NdRu_2Zn_{20}$ was found to be of an isotropic Γ_6 ground state with a Curie temperature of 1.9 K, and the magnetic and thermal properties were well explained by theoretical calculations. [6] We have made single crystals of NdT_2Al_{20} (T = Ti, V, and Cr), in which antiferromagnetic phase transition was observed in $NdTi_2Al_{20}$ at the Néel temperatures T_N = 1.45 K, and NdV_2Al_{20} and $NdCr_2Al_{20}$ ferromagnetically ordered at the Curie temperatures of T_C = 1.8 K and T_C = 1.7 K, respectively. [7] The CEF ground states of Nd^{3+} ions were determined to be doublet Γ_6 for $NdTi_2Al_{20}$ and $NdCr_2Al_{20}$, while the ground state of NdV_2Al_{20} was unclear because of its anomalous thermal behaviors. These interesting results motivated us to systematically study the physical properties of the Nd-based compounds NdT_2Al_{20} (T = transition metals).

In this thesis, we systematically study the magnetic and transport properties of Nd-based compounds NdT_2Al_{20} (T = Ti, V) with Kramers $4f^3$ configurations of Nd^{3+} ions and a new Tm-based system TmV_2Al_{20} with non-Kramers f^{12} configurations of Tm^{3+} ion, with the hope of finding new heavy fermion system in the RT_2X_{20} family.

1.4. Outline of the thesis

This thesis will be presented as follows. With the research background reviewed in this chapter, physics of rare earth magnetism will be briefly introduced in chapter two. In chapter three, experimental methods such as details of the growth of single crystals, the preparation and characterization of the samples, and the measurement techniques of magnetization, specific heat, and electrical resistivity will be introduced. Chapter four will report the detailed experimental results of magnetization, specific heat, and resistivity measurements for the as-

prepared single crystals of $NdTi_2Al_{20}$ as well as the theoretical calculations using the CEF model. The magnetic and transport properties of the NdV_2Al_{20} will be discussed in chapter five with the nonmagnetic single crystals of LaV_2Al_{20} as the reference compound. In chapter six, physical properties of TmV_2Al_{20} single crystals will be presented with analyses of CEF calculations.

2. Theoretical background

In this chapter, physical concepts and theories necessary for the analyses and discussions in the subsequent chapters are briefly reviewed. The physics of rare earth magnetism are introduced in Section 2.1. Section 2.2 is dedicated to the crystalline field effects in cubic symmetry site.

2.1. Localized magnetism of rare earths

The rare earth elements or metals typically include scandium (Sc, atomic number $Z = 21$), yttrium (Y, $Z = 39$) and the fifteen lanthanide elements (Ln) from lanthanum (La, $Z = 57$) to lutetium (Lu, $Z = 71$). By the principle of lowest energy, lanthanide elements adopt either the [Xe]$4f^n6s^2$ or [Xe]$4f^{n-1}5d^16s^2$ configuration, where [Xe] is the electronic configuration of xenon $1s^22s^22p^63s^23p^63d^{10}4s^24p^64d^{10}5s^25p^6$, and n is an integer from 1 to 14. [93]

The magnetism of the rare earths originates from the partially filled 4*f* shells. Figure 2.1 shows the radial wave functions of 4*f*, 5*s*, 5*p*, 5*d*, 6*s*, and 6*p* electrons for Ce, [93] in which the 4*f*-electron shell has a relatively small radius and is shielded from outer disturbances by the full shells of 5*s* and 5*p*. The partially filled 4*f* shells carry magnetic moments. The magnetic moments of the 4*f* shells are localized because of the small radiuses, and the direct interactions between the neighboring 4*f* moments are negligible.

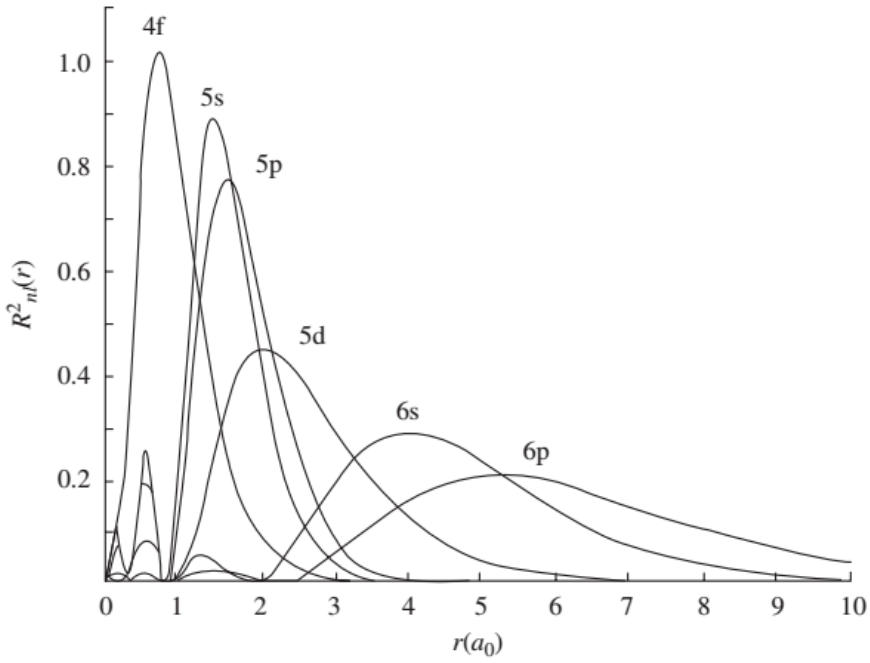

Figure 2.1: Radial wave functions of 4*f*, 5*s*, 5*p*, 5*d*, 6*s*, and 6*p* electrons for Ce. The radius unit is the atomic unit a_0 = 0.529 Å. [93]

The ionization energy of the 4*f* electrons is slightly higher than that of 5*d* electrons, and thus the rare earths usually are trivalent in compounds. However, divalent (Eu, Sm, Tm and Yb) or tetravalent (Ce, Pr, and Tb) configurations may occur in some cases. The atomic radius decreases with increasing atomic number *Z* from La to Lu because of increasing Coulomb attraction between the nuclei and the 4*f* electrons, which is known as the lanthanide contraction (Eu and Yb show irregularity). The electron configurations of the neutral atoms and the trivalent ions, as well as the atomic radiuses for the rare earth elements are shown in Table 2.1. [93]

Table 2.1: The electron configurations and atomic radiuses of the rare earth elements. [93]

Z	Element		Electronic configurations of neutral atoms					Electronic configurations of trivalent ions	Atomic radius (pm) (coordination number = 12)	Atomic weight
			4f	5s	5p	5d	6s			
57	La	The inner	0	2	6	1	2	$[Xe]4f^0$	187.91	138.91
58	Ce	orbitals	1	2	6	1	2	$[Xe]4f^1$	182.47	140.12
59	Pr	have been	3	2	6		2	$[Xe]4f^2$	182.80	140.91
60	Nd	full-filled, 46	4	2	6		2	$[Xe]4f^3$	182.14	144.24
61	Pm	electrons	5	2	6		2	$[Xe]4f^4$	(181.0)	(147)
62	Sm	in all	6	2	6		2	$[Xe]4f^5$	180.41	150.36
63	Eu		7	2	6		2	$[Xe]4f^6$	204.20	151.96
64	Gd		7	2	6	1	2	$[Xe]4f^7$	180.13	157.25
65	Tb		9	2	6		2	$[Xe]4f^8$	178.33	158.93
66	Dy		10	2	6		2	$[Xe]4f^9$	177.40	162.50
67	Ho		11	2	6		2	$[Xe]4f^{10}$	176.61	164.93
68	Er		12	2	6		2	$[Xe]4f^{11}$	175.66	167.26
69	Tm		13	2	6		2	$[Xe]4f^{12}$	174.62	168.93
70	Yb		14	2	6		2	$[Xe]4f^{13}$	193.92	173.04
71	Lu		14	2	6	1	2	$[Xe]4f^{14}$	173.49	174.97
			3d	4s	4p	4d	5s			
21	Sc	Inner 18 electrons	1	2				[Ar]	164.06	44.956
39	Y		10	2	6	1	2	[Kr]	180.12	88.906

2.1.1. Hund's rules

Magnetism of the rare earth element origin in the spin and orbital motion of the electrons in the partially filled 4*f* shells, in which the total spin angular momentum ***S***, the total orbital angular momentum ***L*** and the total angular momentum ***J*** are involved.

Hund's rules can be used to determine the values of total spin angular momentum ***S***, the total orbital angular momentum ***L***, and the total angular momentum ***J*** for the free ion in the ground state as long as we know the number of electrons in the partially filled electron shell. The three rules are [94]:

1) The ground state has the largest total spin $\boldsymbol{S}$ that is consistent with the exclusion principle.
2) The total orbital angular momentum $\boldsymbol{L}$ of the ground state also takes its largest value that is consistent with the exclusion principle and the first rule.
3) For shells that are less than half-filled, the total angular momentum $\boldsymbol{J} = |\boldsymbol{L}-\boldsymbol{S}|$. For shells that are more than half-filled, $\boldsymbol{J} = |\boldsymbol{L}+\boldsymbol{S}|$.

Table 2.2: Ground-state properties of the trivalent rare earth ions. [95]

R^{3+} ion	N	S	L	J	$^{2S+1}L_J$	g_J	$g_J J$, μ_B	$g_J\sqrt{J(J+1)}$, μ_B
La	0	0	0	0	$^1S_0$	-	0.00	0.00
Ce	1	1/2	3	5/2	$^2F_{5/2}$	6/7	2.14	2.54
Pr	2	1	5	4	$^3H_4$	4/5	3.20	3.58
Nd	3	3/2	6	9/2	$^4I_{9/2}$	8/11	3.28	3.62
Pm	4	2	6	4	$^5I_4$	3/5	2.40	2.68
Sm	5	5/2	5	5/2	$^6H_{5/2}$	2/7	0.72	0.84
Eu	6	3	3	0	$^7F_0$	-	0.00	0.00
Gd	7	7/2	0	7/2	$^8S_{7/2}$	2	7.00	7.94
Tb	8	3	3	6	$^7F_6$	3/2	9.00	9.72
Dy	9	5/2	5	15/2	$^6H_{15/2}$	4/3	10.00	10.63
Ho	10	2	6	8	$^5I_8$	5/4	10.00	10.60
Er	11	3/2	6	15/2	$^4I_{15/2}$	6/5	9.00	9.59
Tm	12	1	5	6	$^3H_6$	7/6	7.00	7.57
Yb	13	1/2	3	7/2	$^2F_{7/2}$	8/7	4.00	4.54
Lu	14	0	0	0	$^1S_0$	-	0.00	0.00

Table 2.2 summarizes the ground-state properties of the trivalent rare earth ions, where N is the number of $4f$ electrons of the R^{3+} ion, the Landé factor $g_J = 1 + \frac{J(J+1)+S(S+1)-L(L+1)}{2J(J+1)}$,

the Bohr magneton $\mu_B = \frac{e\hbar}{2m}$, the saturated moment $\mu_{sat} = g_J J \mu_B$, and the effective magnetic moment $\mu_{eff} = g_J \mu_B \sqrt{J(J+1)}$.

2.1.2. Curie law and Curie-Weiss law

The magnetic properties of a system can be determined by quantum numbers of the atoms and the numbers of atoms *N* in the system.

When a magnetic field (***H***) is applied along the quantization direction (*z*-axis), the degeneracy of the ground state will be split into 2*J*+1 equally spaced energy levels and the overall splitting is proportional to the applied field. The energies of these 2*J*+1 levels are

$$E_H = -\mu_0 \boldsymbol{\mu} \cdot \boldsymbol{H} = -\mu_0 \mu_z H = \mu_0 g_J m \mu_B H, \tag{2.1}$$

The magnetization of a system depends on how the energy levels of the atoms are occupied. For instance, at temperature of absolute zero, only the lowest level for each of the N atoms is occupied, therefore, the magnetization of the system

$$M = -N g_J J \mu_B. \tag{2.2}$$

At nonzero temperatures, how higher energy levels will be occupied depends on both the temperature and the magnetic field. The relative population of each level in an applied field of *H* at the temperature of *T* can be estimated by the Boltzmann distribution, and the probability of finding an atom with energy E_i is given by

$$P_i = \frac{\exp(-E_i/k_B T)}{\sum_i \exp(-E_i/k_B T)}, \tag{2.3}$$

Then, the magnetization M can be obtained from the statistical average $\langle \mu_z \rangle$ of the magnetic moment $\mu_z = g_J m \mu_B$ for all the N atoms in the system:

$$M = N\langle \mu_z \rangle = N \frac{\sum_{m=-J}^{J} -g_J m \mu_B \exp\left(-\frac{g_J m \mu_0 \mu_B H}{k_B T}\right)}{\sum_{m=-J}^{J} \exp\left(-\frac{g_J m \mu_0 \mu_B H}{k_B T}\right)} = N g \mu_B \frac{d}{dx}\left(\ln \sum_{m=-J}^{J} e^{mx}\right), \quad (2.4)$$

where $x = g_J m \mu_0 \, \mu_B \, H/k_B T$, and $g \equiv g_J$. With some mathematical treatments of Equation (2.4) we may find

$$M = N g \mu_B J B_J(y) , \quad (2.5)$$

in which the Brillouin function

$$B_J(y) = \frac{2J+1}{2J} coth \frac{(2J+1)y}{2J} - \frac{1}{2J} coth \frac{y}{2J} , \quad (2.6)$$

and

$$y = \frac{gJ\mu_B \mu_0 H}{k_B T} . \quad (2.7)$$

Equation (2.5) can be much simpler in low magnetic fields at high temperatures. For instance, with J = 9/2 and g = 8/11, the y value of Nd^{3+} in an external field of 0.1 T at room temperature (298 K) is determined to be 0.00074 by adopting Equation (2.7) and the relevant physical constants of Bohr magneton $\mu_B = 9.274 \times 10^{-24}$ J·T^{-1} and the Boltzmann constant $k_B = 1.380 \times 10^{-23}$ J·K^{-1}.

As we can see, the y value is far less than 1 ($y = 0.00074 \ll 1$) in the above mentioned condition, in this case we can use only the first term of series expansion of the Brillouin function. Since

$$B_J(y) = \frac{J+1}{3J} y - \frac{[(J+1)^2 + J^2](J+1)}{90J^3} y^3 + O(y^5), \quad (2.8)$$

the magnetization M can be obtained,

$$M = Ng\mu_B J B_J(y) = Ng\mu_B J \cdot \frac{J+1}{3J} \cdot \frac{gJ\mu_B\mu_0 H}{k_B T} = \frac{N\mu_0 g^2 J(J+1)\mu_B^2 H}{3k_B T}. \quad (2.9)$$

The magnetic susceptibility defined as $\chi = M/H$ can be obtained from Equation (2.9),

$$\chi = \frac{M}{H} = \frac{N\mu_0 g^2 J(J+1)\mu_B^2}{3k_B T} = \frac{N\mu_{eff}^2}{3k_B} = \frac{C}{T}, \quad (2.10)$$

and the Curie constant

$$C = \frac{N\mu_0 g^2 J(J+1)\mu_B^2}{3k_B}, \quad (2.11)$$

Equation (2.10) is known as Curie's law, and the associated effective moment

$$\mu_{eff} = g\sqrt{J(J+1)}\mu_B . \quad (2.12)$$

Note that Curie law is the result of the thermal average involving only the $2J+1$ equally spaced levels when a magnetic field is applied on one multiplet level. Deviations from Curie law may occur when more than $2J + 1$ levels are involved or when the energy levels are not equally spaced. The electrostatic fields or the crystalline electric field (CEF) can lead to the latter situation, which will be discussed in the next section.

Interactions between the magnetic moments are neglected in deriving the Curie`s law, as have been described above. These interactions are taken into account within the model of the molecular field, in which an effective field (the molecular field) $H_m = \alpha M$ is added to the external applied field H. In this case, the magnetization

$$M = \frac{C}{T}(H + H_m) = \frac{C}{T}(H + \alpha M). \quad (2.13)$$

Therefore, the magnetic susceptibility can be written as

$$\chi = \frac{M}{H} = \frac{C}{T-\alpha C} = \frac{C}{T-\theta_P} = \frac{N\mu_{eff}^2}{3k_B(T-\theta_p)}. \quad (2.14)$$

which is known as the Curie-Weiss law, and θ_P is paramagnetic Curie temperature.

The inverse susceptibility is linear at high temperatures, which allows us to determine θ_p and μ_{eff} experimentally by a linear fitting of the H / M vs T curve.

2.1.3. Kondo effect and RKKY interaction

A single magnetic impurity in a nonmagnetic metal host may couple with the conduction electrons through exchange interaction and lead to the so-called single-ion Kondo effect, in which the local moment tends to be screened by the conduction electrons. It can be used to explain the local minimum and the subsequent logarithmic increase in the electrical resistivity with decreasing temperature in dilute magnetic alloys. [96,97]

The single-ion Kondo effect is usually found in diluted compounds with a small amount of magnetic impurities, in which the magnetic moments do not interact with each other, directly or indirectly, because of the large distance between them. When the localized magnetic moments completely occupy a lattice site and form a Kondo lattice (Heavy Fermion system), the distance between the neighboring magnetic moments is relatively small. In this case, although the direct Coulomb interaction between the magnetic moments is still negligible, they may interact indirectly via the so-called Ruderman-Kittel-Kasuya-Yosida (RKKY) interaction mediated by the spin polarization of the conduction electrons.

In the rare earth intermetallic compounds, the Kondo effect and RKKY interaction compete with each other. The RKKY interaction enhances the long-range magnetic order,

while the Kondo effect favors a nonmagnetic ground state and tend to quench the magnetic moments. Doniach's phase diagram [98], as shown in Figure 2.2, can be used to illustrates the competition between the Kondo effect and the RKKY interaction. The characteristic temperatures of the Kondo effect T_{K}, RKKY interaction T_{RKKY}, and the magnetic ordering temperature T_{mag} are displayed as a function of $J_{cf}D(\varepsilon_F)$, where J_{cf} is the exchange interaction between the magnetic moment and conduction electrons, and $D(\varepsilon_F)$ is the electronic density of states (DOS) at the Fermi energy ε_F. The characteristic temperatures are given by: $T_{RKKY} \propto \left|J_{cf}\right|^2 D(\varepsilon_F)$ and $T_K \propto \exp(-\frac{1}{|J_{cf}|D(\varepsilon_F)})$. [99]

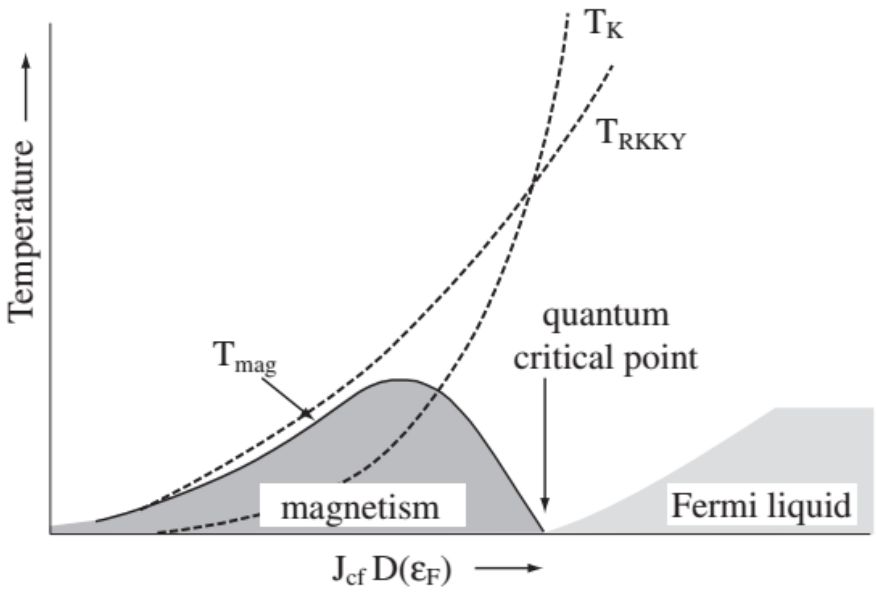

Figure 2.2: Doniach's phase diagram. [98]

When the parameter $J_{cf}D(\varepsilon_F)$ is small, the Kondo effect is negligible, the RKKY interaction dominates and a magnetically ordered stated is formed. As $J_{cf}D(\varepsilon_F)$increases, the

Kondo effect become more important, but magnetic ordering state is still observed in low temperature region.

When Kondo effect and RKKY interaction are of the same order of magnitude, heavy-fermion behaviors can be observed. Since T_K increases faster than T_{RKKY}, the ordering temperature T_{mag} will drop after a local maximum and thus lead to a quantum phase transition at 0 K. Experimentally, such a quantum critical point (QCP) can be realized at $J_{cf}D(\varepsilon_F) = J_{cf}D_c(\varepsilon_F)$ by chemical substitution or by controlling non-thermal parameters such as pressure and magnetic field. Non-Fermin liquid (NFL) behavior can often be observed near the QCP. The QCP is where the transition between a magnetic state and a paramagnetic Fermi liquid state occurs. When the parameter $J_{cf}D(\varepsilon_F)$ is large, the Kondo effect become dominant, resulting in paramagnetic Fermi liquid (FL) ground state. [100]

2.2. Crystalline electric field effects

Apart from the magnetic fields, electrostatic fields from the surrounding ions (ligands), which is known as crystalline electric field (CEF), can also lift the (2*J*+1)-fold degeneracy of the Hund's rules ground state for rare earth ions and thus affect their magnetic properties in solids at low temperatures. The crystalline electric field has a symmetry determined by the crystal structure, and is able to orient the electronic charge cloud into an energetically favorable direction. [101]

The CEF has a great influence on transition metals with partially filled 3*d* shell, and an energy sequence of CEF > *LS* coupling (Russel-Saunders) > applied magnetic field was

involved in the formation of the electronic states. The CEF may quench the orbital contribution to the total magnetic moment. However, the CEF splitting of the localized 4*f* shell of rare earths or 5*f* shell of actinide is relatively small: *LS* coupling > CEF > applied magnetic field, so that it can be seen as a perturbation that lift the (2*J*+1)-fold ground state degeneracy of free ions. Furthermore, CEF can lead to magnetic anisotropy in the intermetallic compounds.

2.2.1. Stevens equivalent operators

The crystal-field potential due to the surrounding ions at the site of the magnetic ion is

$$V_{CEF}(\boldsymbol{r}) = |e| \int \frac{\rho(\boldsymbol{R})}{|\boldsymbol{r}-\boldsymbol{R}|}, \tag{2.15}$$

where $\rho(\boldsymbol{R})$ is the charge density of the surrounding electrons and nuclei. Since the surrounding charges causing the crystal field are outside the electron shells of the central rare earth ions, the CEF potential V_{CEF} satisfies the Laplace equation,

$$\nabla V_{CEF} = 0 , \tag{2.16}$$

and can be expanded in spherical harmonics $Y_n^m(\theta, \varphi)$ as

$$V_{CEF} = \sum_{n=0}^{\infty} \sum_{-n}^{n} A_n^m r^n Y_n^m(\theta, \varphi) . \tag{2.17}$$

Here, A_n^m are the CEF coefficients, the values of which depend on the crystal structure and determine the strength of the CEF interaction.

For 4*f* configuration with total angular momentum *J*, the matrix elements due to the CEF energy are

$$\langle JM_i|A_n^m r^n Y_n^m(\theta,\varphi)|JM_k\rangle = A_n^m\langle R|r^n|R\rangle\langle\Phi_i|Y_n^m(\theta,\varphi)|\Phi_k\rangle\ . \quad (2.18)$$

The wave function $|\Phi\rangle$ can be expanded in spherical harmonic functions up to n =3 for the f electrons (l = 3), and all the terms of $\langle\Phi_i|Y_n^m(\theta,\varphi)|\Phi_k\rangle$ with n > 6 will be vanish. Furthermore, n cannot be odd number owing to inversion symmetry of the crystal-field potential, which means that n = 2, 4, 6 for the f electrons.

The CEF Hamiltonian can be expressed by using Stevens Operator Equivalents method [102].

$$\mathcal{H}_{CEF} = \sum_{n,m} A_n^m\langle r^n\rangle\,\theta_n O_n^m = \sum_{n,m} B_n^m\,O_n^m, \quad (2.19)$$

where O_n^m are Stevens equivalent operators, $\langle r^n\rangle$ is the expectation of the 4f radius, $B_n^m = A_n^m\langle r^n\rangle\theta_n$, the reduced matrix elements θ_n are often called α_J, β_J, and γ_J for n = 2, 4, and 6 respectively. For magnetic ions with given J values, the operator equivalents O_n^m are known. A complete list of values of O_n^m , α_J, β_J, and γ_J can be found in Hutchings' paper [103]. The eigenvalues of the CEF states can be calculated by diagonalization of the matrix elements.

2.2.2. Crystalline electric field in cubic symmetry

The CEF Hamiltonian in cubic symmetry have been investigated by Lea *at el*. [104] The CEF Hamilton can be written as

$$\mathcal{H}_{\mathrm{CEF}} = B_4(O_4^0 + 5O_4^4) + B_6(O_6^0 - 21O_6^4)\ , \quad (2.20)$$

where the quantization axis is chosen along the fourfold axis of symmetry in the cubic. The coefficients B_4 and B_6 determine the scale of the CEF splitting, and they are in proportion to $\langle r^4\rangle$ and $\langle r^6\rangle$ of the 4f electrons. In principle, the CEF parameters can be calculated by

using the point charge model. However, the calculated results sometimes can be of one order of magnitude difference compared with the experimental results, due to the surrounding charge density and shielding effects of conduction electrons on the CEF, which are hard to estimate. Therefore, the crystal field parameters B_n^m(B_4 and B_6) are usually determined by experimental results.

In order to keep the eigenvalues in the same numerical range and cover all possible values of the ratio between the fourth and sixth degree terms, the Hamiltonian is written as

$$\mathcal{H}_{\mathrm{CEF}} = W\left(x\frac{O_4}{F(4)} + (1-|x|)\frac{O_6}{F(6)}\right). \tag{2.21}$$

Here, $Wx = B_4F(4)$, $W(1-|x|) = B_6F(6)$; $O_4 = [O_4^0 + 5O_4^4]$, $O_6 = [O_6^0 - 21O_6^4]$; $F(4)$ and $F(6)$ are normalizing parameters of the total angular moment J; W and x ($-1 < x < +1$) are two parameters of the CEF effect energy scale and the relative importance of the fourth and sixth degree terms, respectively. [104]

In the cubic RT_2X_{20} system, the Hamiltonian for local moment of R^{3+} ion can be written as

$$\mathcal{H} = \mathcal{H}_{\mathrm{CEF}} + \mathcal{H}_{\mathrm{Z}} + \mathcal{H}_{\mathrm{exch}}, \tag{2.22}$$

where $\mathcal{H}_{\mathrm{CEF}}$ is the crystalline-electric-field Hamiltonian, $\mathcal{H}_{\mathrm{Z}}$ is the Zeeman Hamiltonian of magnetic field, and $\mathcal{H}_{\mathrm{exch}}$ is the exchange interaction Hamiltonian between R^{3+} ions.

Based on the work of Lea *et al* [104], we reproduced the CEF schemes of trivalent rare earth ions Nd^{3+} and Tm^{3+} in cubic symmetry when W = 1 K, which will be frequently used for the analyses of CEF effects in subsequent chapters, as shown in Figure 2.3 and Figure 2.4, respectively.

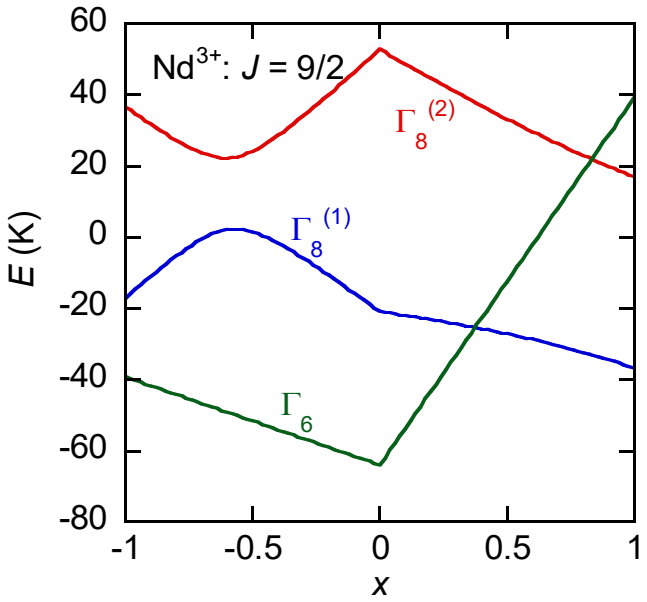

Figure 2.3: Energy schemes of Nd^{3+} ion when $W = 1$ K.

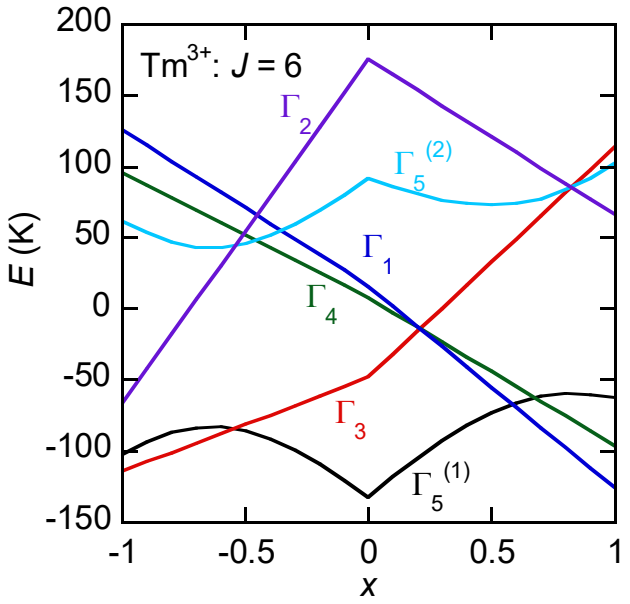

Figure 2.4: Energy schemes of Tm^{3+} ion when $W = 1$ K.

3. Experimental methods

3.1. Sample preparation

All the single crystal samples used in this study were prepared by arc-melting method under an argon atmosphere followed by a subsequent Al self-flux method. The structures of the as-prepared samples were determined by X-ray powder diffraction using pulverized single crystals. The crystallographic orientations of the single crystals were done by Laue back reflection of X-rays. Well oriented single crystals are used for further anisotropic measurements of magnetic and transport properties.

3.1.1. Growth of single crystal

Intermetallic compounds comprise exclusively of different metals or metalloids. Arc-melting and induction heating are often used to melt the elemental components at very high temperatures to get polycrystalline samples of intermetallic compounds. Polycrystalline samples can be used for some measurements, but they cannot provide anisotropic information and impurities are easy to form at the grain boundaries. The growth of high quality single crystal is important for detailed studies of the anisotropic properties and the crystalline-electric-field (CEF) effects.

Single crystals can be made by many techniques, such as Czochralski method [105], Bridgeman method [106], and Zone Melting [107], all with their advantages and disadvantages. These methods can be used to grow large single crystals, but usually they are

not suitable for incongruently melting compounds and a seed crystal is needed. What's more, the starting components must be heated up to the melting temperatures of the target compound at which the vapor pressures of the constituent elements might be fairly large.

The flux method in which molten solids are used as solvents (i.e. fluxes) is one of the most versatile methods for single crystal growth free from many of the problems mentioned above [108,109]. The flux method has been widely used for growing intermetallic single crystals, and the main advantages of this method are the enhanced diffusion of the component elements in metal solvents and relatively lower reaction temperatures. A metal has some typical features to be a flux: 1) the metal should form a flux (i.e. a melt) at low temperatures that the heating equipment and containers can bear, 2) a large difference between the melting and boiling point, 3) the metal can be separate from the products, 4) the metal flux should not form highly stable binary compounds with any of the reactants. [108] The metal fluxes vary greatly, including but not limited to aluminum (Al), gallium (Ga), indium (In), tin (Sn), lead (Pb), bismuth (Bi), zinc (Zn), cadmium (Cd), mercury (Hg), lithium (Li), sodium(Na), calcium (Ca) and some miscellaneous metallic fluxes (Cu-Al fluxes and Ti/Al/Sn fluxes). [108–113]

The elemental components are dissolved in the flux at high temperatures. As the temperature decreases, the target compounds will crystallize from the solution because of the decreases of the solubility. In many cases, the fluxes act as both solvents and reactants, providing atoms to the target compounds. In our case, the ternary aluminides RT_2Al_{20} were prepared using excessive aluminum as reactive fluxes (i.e. Al self-flux).

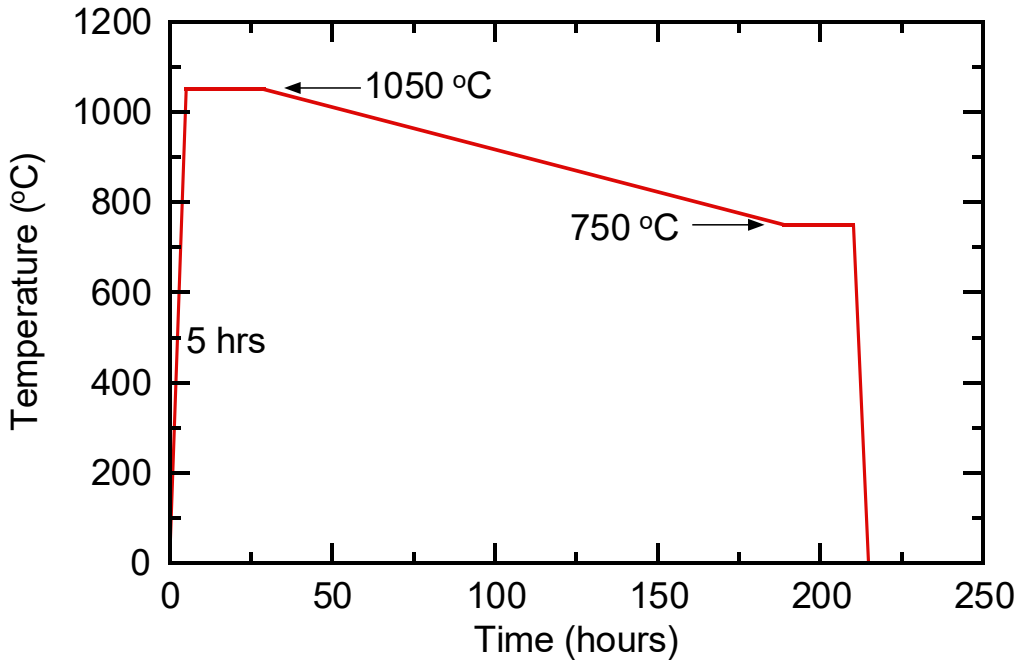

Figure 3.1: Temperature profile for the growth of single crystals from Al flux.

In a typical Al self- flux method, a polycrystalline sample with the stoichiometric ratio of *R*: *T*: Al = 1:2:20 is preliminarily prepared by arc-melting using a tungsten electrode under an argon atmosphere. The sample is turned and melt more than six times for homogeneity on a water-cooled copper hearth. Then the sample is put into alumina crucible with some Al ingots / shots to reach a mole ratio of *R*: *T*: Al = 1:2:50 (the content of Al may differ in some cases), and is sealed into a vacuum silica tube. The sample sealed in the silica tube was heated up to 1050 ℃ in 5 hours, kept for 4 – 24 hours at 1050℃, and then slowly cooled down to 750 ℃ within 80 – 160 hours. The heat treatment process for the growth of single crystals from Al flux is illustrated in Figure 3.1.

Single crystals with typical dimensions of several millimeters are obtained by centrifuging out the excess Al flux at 750 ℃ before cooling down. Small amount of residual Al flux on the single crystal surface is removed by dilute hydrochloric acid (HCl) in an ultrasonic bath. Figure 3.2 shows the obtained single crystals of TmV_2Al_{20} with the typical shape and dimensions.

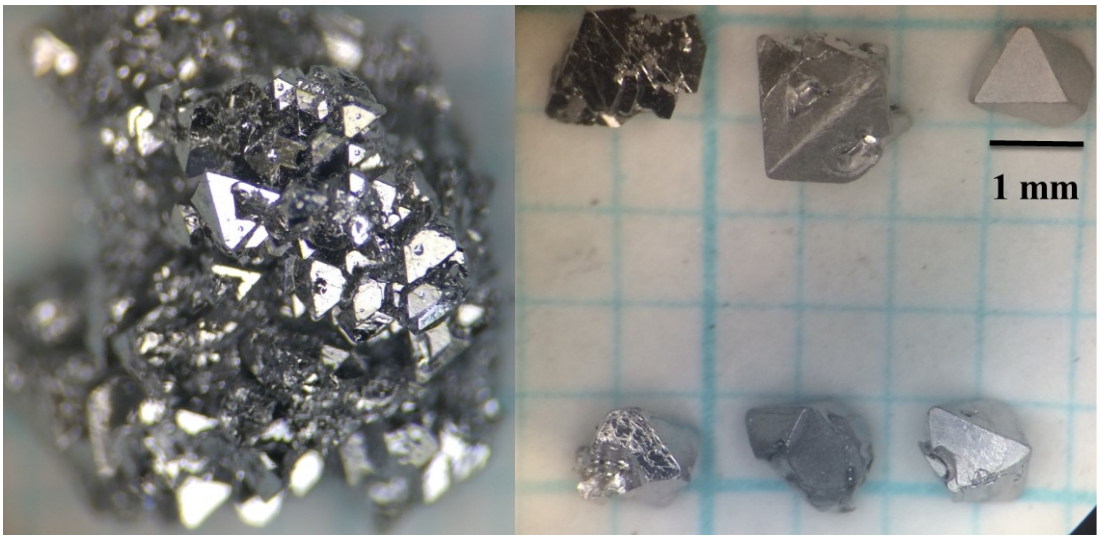

Figure 3.2: Single crystals of TmV_2Al_{20} with the typical shape and dimensions.

3.1.2. Powder X-ray diffraction

X-ray diffraction experiments were performed on pulverized single crystals in a Rigaku RINT 2200 diffractometer with monochrome Cu-Kα radiation (λ = 1.5405 Å) at room temperature. In typical measurements, the working voltage and current were 40 kV and 20 mA, respectively. The diffraction data were collected for $10^o \leq 2\theta \leq 90^o$ with a scanning step of 0.02° and a scan speed of 2^o / min.

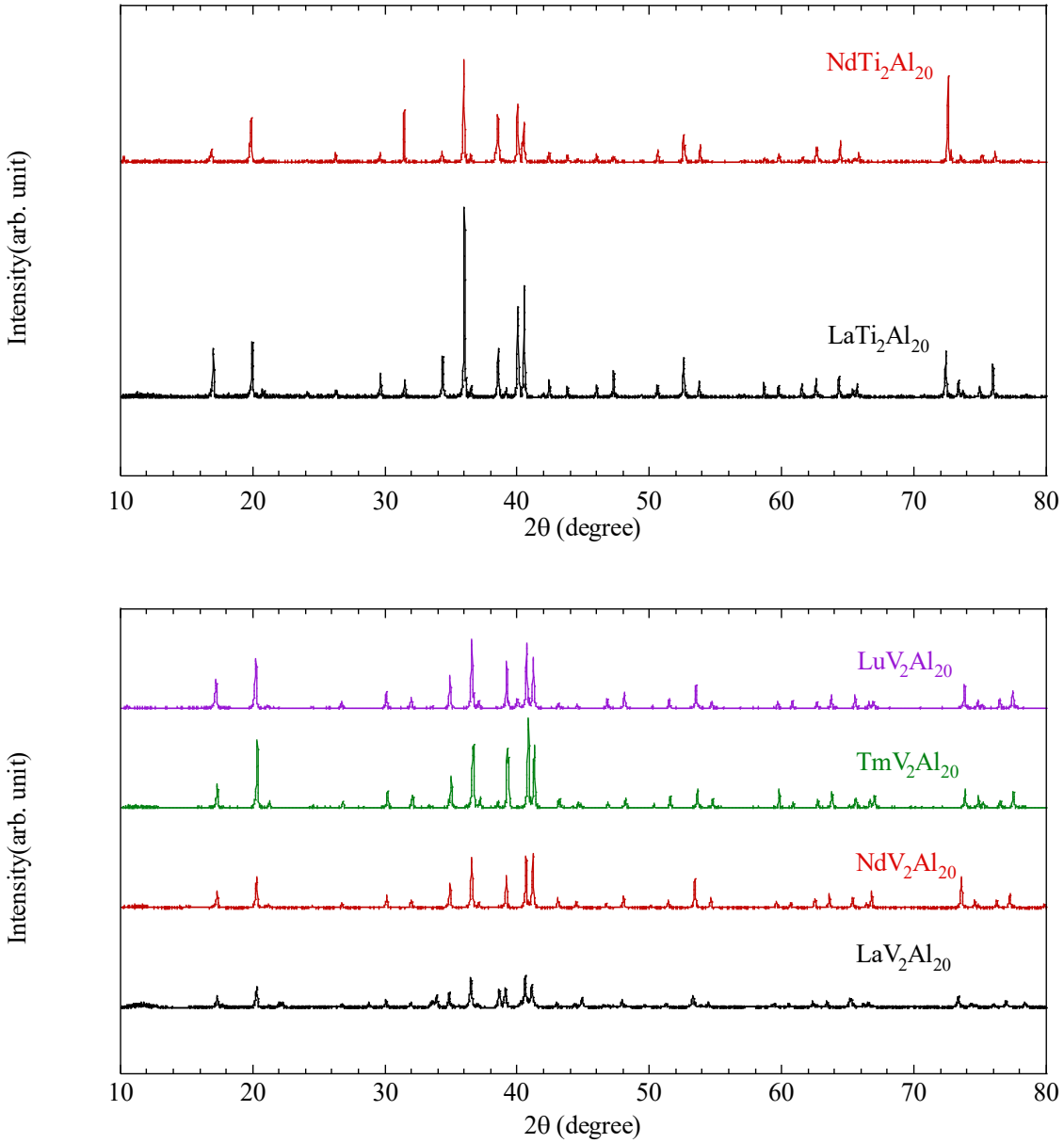

Figure 3.3: XRD patterns of RT_2Al_{20} (R = La, Nd, Tm, Lu, T =Ti, V).

The XRD patterns are displayed in Figure 3.3, in which no impurity phases were found and all the peaks can be indexed as the $CeCr_2Al_{20}$-type cubic structure (space group $Fd\bar{3}m$). The diffraction patterns were refined to obtain the lattice parameters. The observed lattice

parameters of RT_2Al_{20} (R = Ti, V) of the as-prepared samples and those in the previous reports are shown Figure 3.4. [1,55] All the experimental lattice parameters are close to the reported ones. Lanthanide contraction effect was observed, and the lattice parameters of RV_2Al_{20} are smaller than their Ti counterparts.

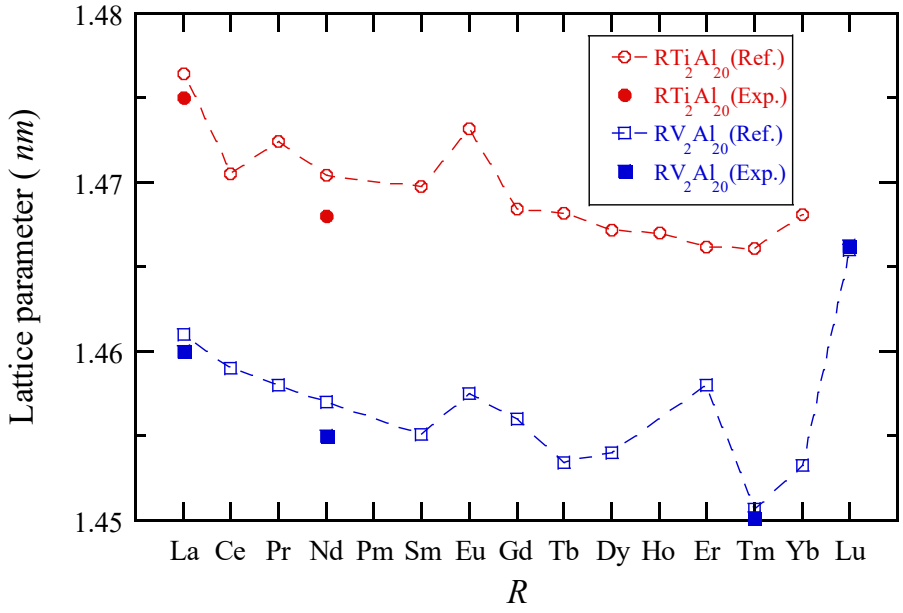

Figure 3.4: Lattice parameters of RT_2Al_{20} (R = rare earth, T = Ti, V).

3.1.3. Single crystal orientation

Orientation of the crystals were determined by Laue back-reflection of X-rays. In a typical measurement, the distance between the oriented crystal and the film was set D = 3.0 cm. The symmetry of the single crystals and directions of the crystal axes can be determined by the Laue pattern, since the symmetry of the singe crystal observed along the X-ray direction is the same as that of the Laue pattern.

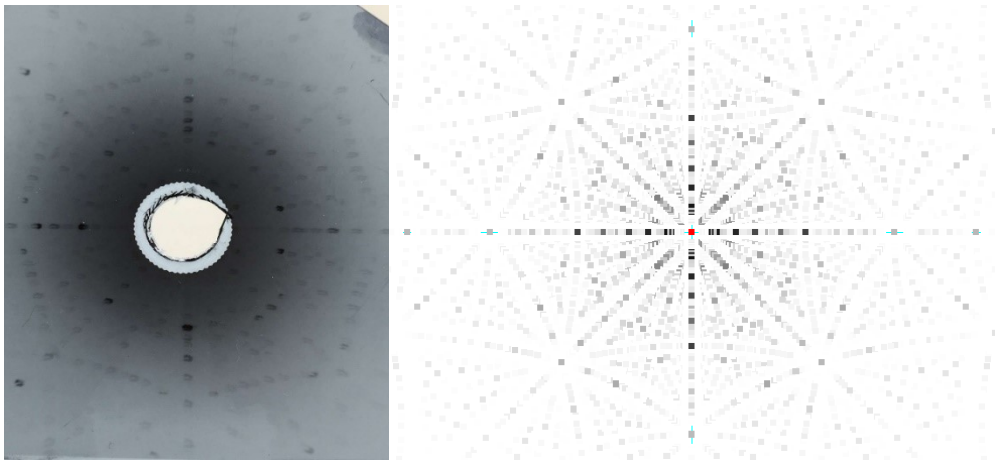

Figure 3.5: The Laue pattern of NdV_2Al_{20} single crystal with the [100] direction perpendicular to the film is shown on the left-hand side, and the calculated Laue pattern is shown on the right-hand side.

Laue patterns for [100], [110], and [111] axes are of four-, two-, and three-fold symmetry respectively for the cubic structure single crystals in our case. The Laue pattern of NdV_2Al_{20} single crystal with the [100] direction perpendicular to the film as well as the calculated Laue pattern is displayed in Figure 3.5, which shows a four-fold symmetry. We use [100], [110], and [111] axes for <100>, <110>, and <111> axes, respectively throughout this thesis, since theoretically the measurable proprieties along these directions are the same, respectively, in the cubic-structure compounds.

3.2. Measurements of physical properties

3.2.1. Magnetization measurement

The magnetization measurements were carried out in a commercial superconducting quantum interference device (SQUID) magnetometer, the magnetic properties measurement

system (MPMS) from Quantum Design, in the temperature range of 0.5 – 300 K and DC external magnetic fields up to 7 T.

3.2.2. Specific heat measurement

The specific heat measurements were performed in a physical property measurement system (Quantum Design, PPMS-9) with the heat capacity option by the thermal relaxation method down to 0.5 K and up to 9 T.

3.2.3. Electrical resistivity measurement

The electrical resistivity measurements were carried out in the temperature range of 1.9 – 300 K by the standard DC four-probe method with alternative current in order to eliminate the thermoelectric voltage in the sample using the resistivity option of the physical property measurement system (PPMS) from Quantum Design.

4. Antiferromagnetic ordering in $NdTi_2Al_{20}$ single crystals

4.1. Experimental results

4.1.1. Magnetic properties

Figure 4.1(a) shows temperature dependence of the magnetic susceptibility for $NdTi_2Al_{20}$ in an applied field of 0.1 T along the [110] direction on a logarithmic temperature scale, in which an antiferromagnetic (AFM) phase transition was observed at the Néel temperature T_N = 1.4 K. Figure 4.1(b) shows the corresponding H / M plot, and the high temperature data are almost linear and follow the Curie-Weiss law $\chi = \frac{M}{H} = N\mu_{eff}^2/3k_B(T-\theta_p)$. The effective magnetic moment μ_{eff} = 3.56 μ_B and the Curie-Weiss temperature θ_P = − 28.50 K were obtained by a linear fitting to the Curie-Weiss law in the temperature range from 100 to 300 K. The experimental value of the effective moment 3.56 μ_B is close to that of the free ion Nd^{3+} (3.64 μ_B), which indicates the localized nature of Nd^{3+} ion in $NdTi_2Al_{20}$. The negative value of Curie-Weiss temperature corresponds to the antiferromagnetic interactions between Nd moments. As shown in Figure 4.1(b), the inverse susceptibility H / M deviates from the linear fitting at low temperatures, which can be ascribed to the magnetic interactions and CEF effects.

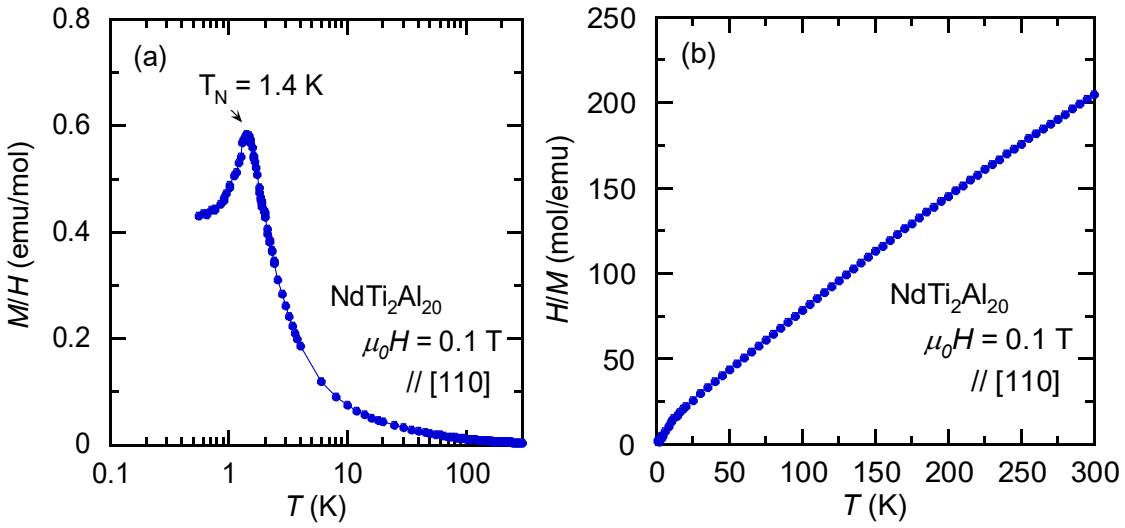

Figure 4.1: Temperature dependences of (a) the magnetic susceptibility M / H on a logarithmic temperature scale, and (b) the inverse magnetic susceptibility H / M in an applied field of 0.1T along the [110] direction for $NdTi_2Al_{20}$.

Figure 4.2(a) and Figure 4.2(b) display field dependences of magnetization for the three principal crystallographic axes [100], [110], and [111] at 0.5 K, in which neither magnetic anisotropy nor hysteresis was found within experimental errors. The magnetizations at 7 T are about 1.4 μ_B/Nd, which are only 40% of the saturation moment of Nd^{3+} ion, μ_{sat} = 3.28 μ_B. The reduction of moment can be attributed to the CEF effects. The field dependences of magnetization at constant temperatures of 0.5, 1.9, 5.0, and 10.0 K in applied magnetic fields along [110] are shown in Figure 4.2(c) and Figure 4.2(d). Metamagnetic transitions were observed at 0.5 K in applied field around 0.16 T along all the three principal axes, as can be seen from Figure 4.2(b) and Figure 4.2(d).

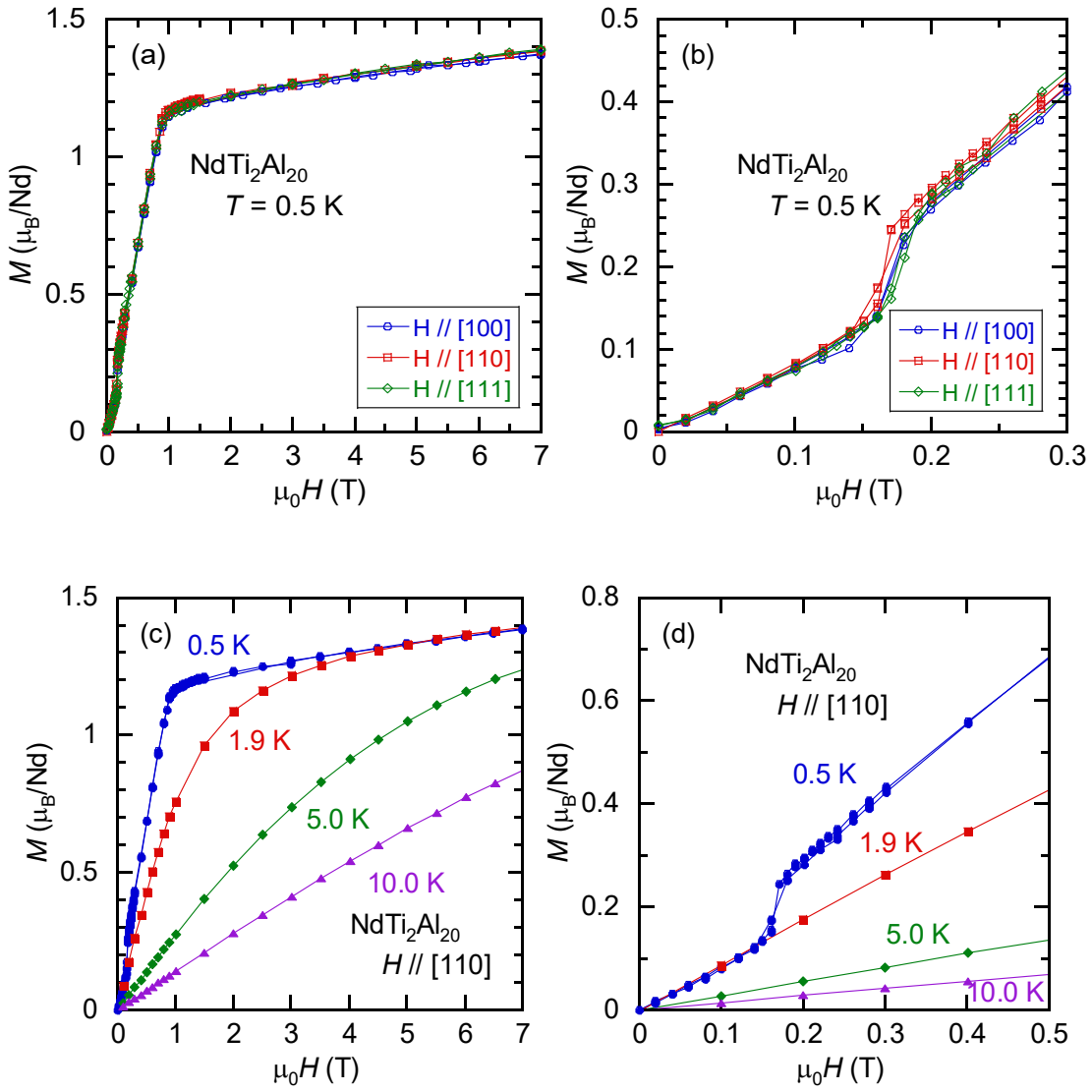

Figure 4.2: Field dependences of magnetization along the three principal crystallographic axes [100], [110], and [111] at $T = 0.5$ K in applied fields (a) up to 7 T, (b) from 0 to 0.3 T for $NdTi_2Al_{20}$. Field dependences of magnetization at various temperatures in applied magnetic fields along [110] (c) up to 7 T, and (d) from 0 to 0.5 T for $NdTi_2Al_{20}$.

4.1.2. Specific heat and magnetic entropy

The specific heats C of $NdTi_2Al_{20}$ in applied fields of 0, 1, 3, 6, and 9 T along the [110] direction and the specific heat of and the nonmagnetic reference compound $LaTi_2Al_{20}$ were plotted on a logarithmic temperature scale, as shown in Figure 4.3(a). In applied fields above 1 T, the peak of specific heat shifts to higher temperature region and become broader with increasing applied field, corresponding to the Schottky anomaly.

Specific heats of the single crystals of $NdTi_2Al_{20}$ were measured at temperatures from 0.5 to 300 K in applied fields up to 9 T. Figure 4.3(b) shows temperature dependences of specific heat C for single crystal of $NdTi_2Al_{20}$ in small applied fields below 1 T along the [110] direction on a linear temperature scale. A sharp peak of the specific heat was observed near 1.4 K in zero field, confirming the AFM transition that has been observed in the temperature dependence of magnetic susceptibility as shown in Figure 4.1(a). The peak of the specific heat for $NdTi_2Al_{20}$ shifts to lower temperature region with increasing applied field below 1 T, which is a typical behavior of the AFM ordering materials. The peak of C splits into two peaks in applied field of 0.4 T and 0.6 T.

The specific heat of $LaTi_2Al_{20}$ in zero field is much smaller than that of $NdTi_2Al_{20}$ at low temperatures as shown in Figure 4.3(a). With a C / T vs T^2 plot using the data in the temperature range from 1.9 to 4 K, the electronic specific heat coefficient γ and the Debye temperature Θ_D are estimated to be 21 mJ/(mol·K^2) and 537 K for $LaTi_2Al_{20}$, respectively, which are close to the reported ones. [53] The magnetic part of specific heat for $NdTi_2Al_{20}$ C_{mag} is estimated using $C_{mag} = C\ (NdTi_2Al_{20}) - C\ (LaTi_2Al_{20})$.

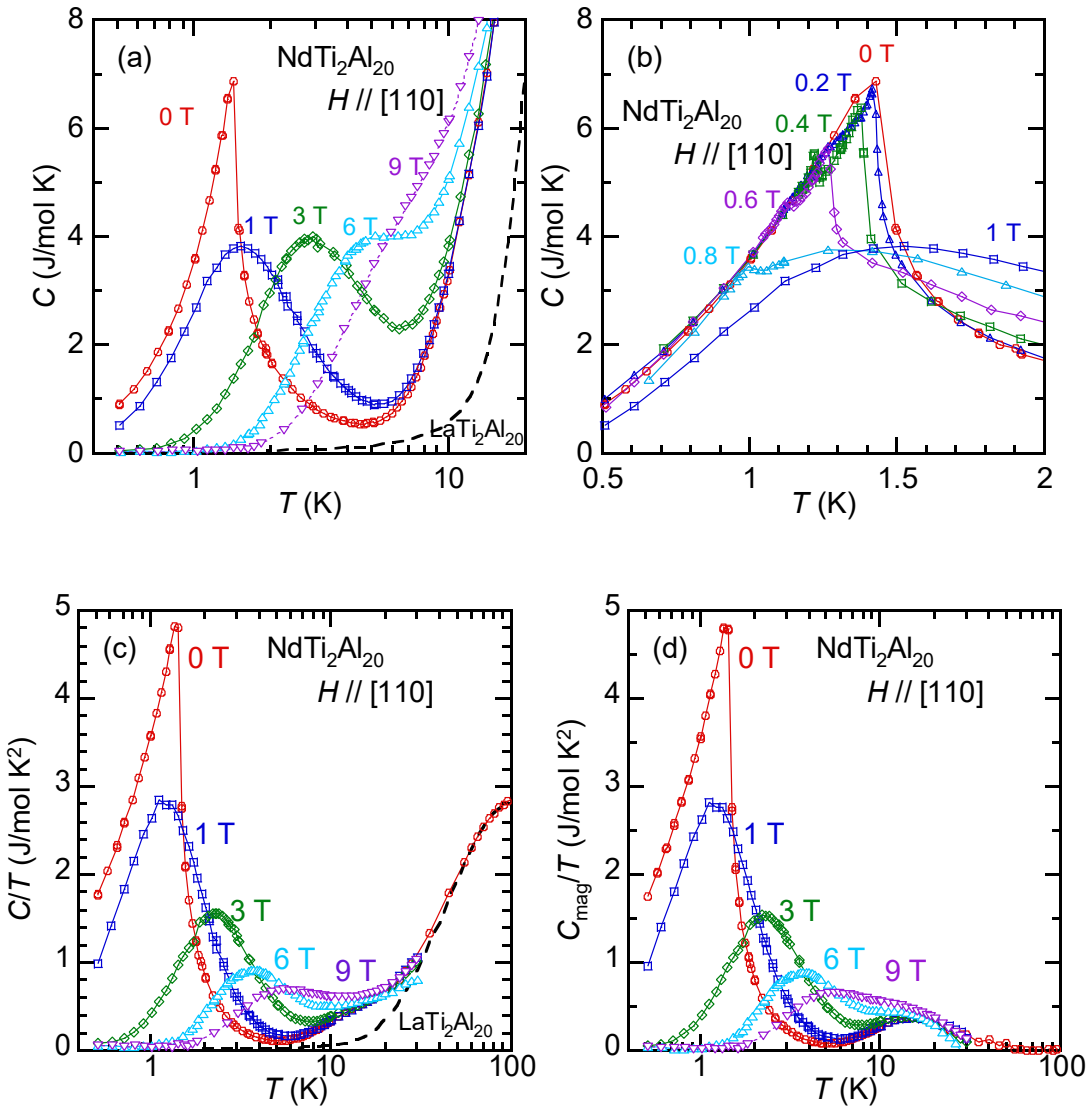

Figure 4.3: Temperature dependences of (a) specific heat C in applied fields of 0, 1, 3, 6, and 9 T on a logarithmic temperature scale, (b) specific heat C for single crystal of $NdTi_2Al_{20}$ in small applied fields below 1 T on a linear temperature scale, (c) specific heat divided by temperature C / T, and (d) magnetic specific heat divided by temperature C_{mag} / T in applied fields of 0, 1, 3, 6, and 9 T on a logarithmic temperature scale for single crystal of $NdTi_2Al_{20}$. The applied fields are along the [110] direction, and the dashed lines denote the specific heat of the nonmagnetic reference compound $LaTi_2Al_{20}$ in zero field.

The C / T plots and C_{mag} / T plots were displayed in Figure 4.3(c) and Figure 4.3(d) on a logarithmic temperature scale, respectively. The peaks become broader and the peak position shifts to higher temperature region with increasing applied fields above 1 T.

Based on the specific heat data in Figure 4.1(b), the corresponding magnetic phase diagram for single crystal of $NdTi_2Al_{20}$ in applied fields along the [110] direction was plotted, as shown in Figure 4.4.

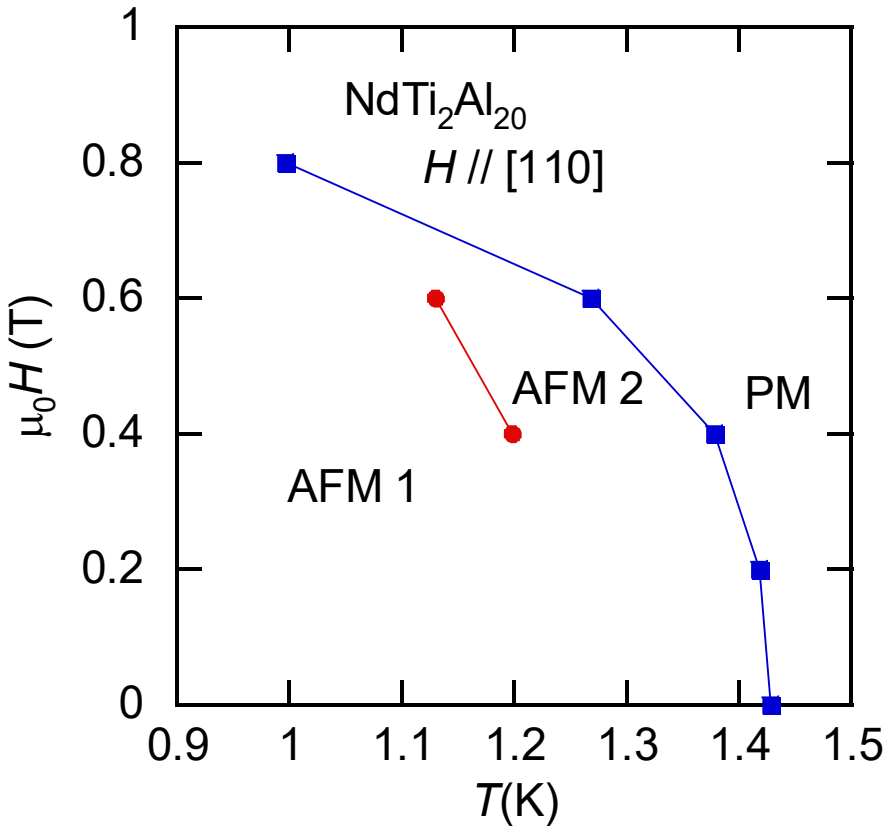

Figure 4.4: Magnetic phase diagram for single crystal of $NdTi_2Al_{20}$ in applied fields along the [110] direction.

Figure 4.5 shows the magnetic entropy S_{mag} of $NdTi_2Al_{20}$ in various applied fields along the [110] direction, which were derived from the experimental data of the specific heats by $S_{mag} = \int_0^T \frac{C_{mag}}{T} dT$, where C_{mag} is the magnetic part of the specific heat for $NdTi_2Al_{20}$. The

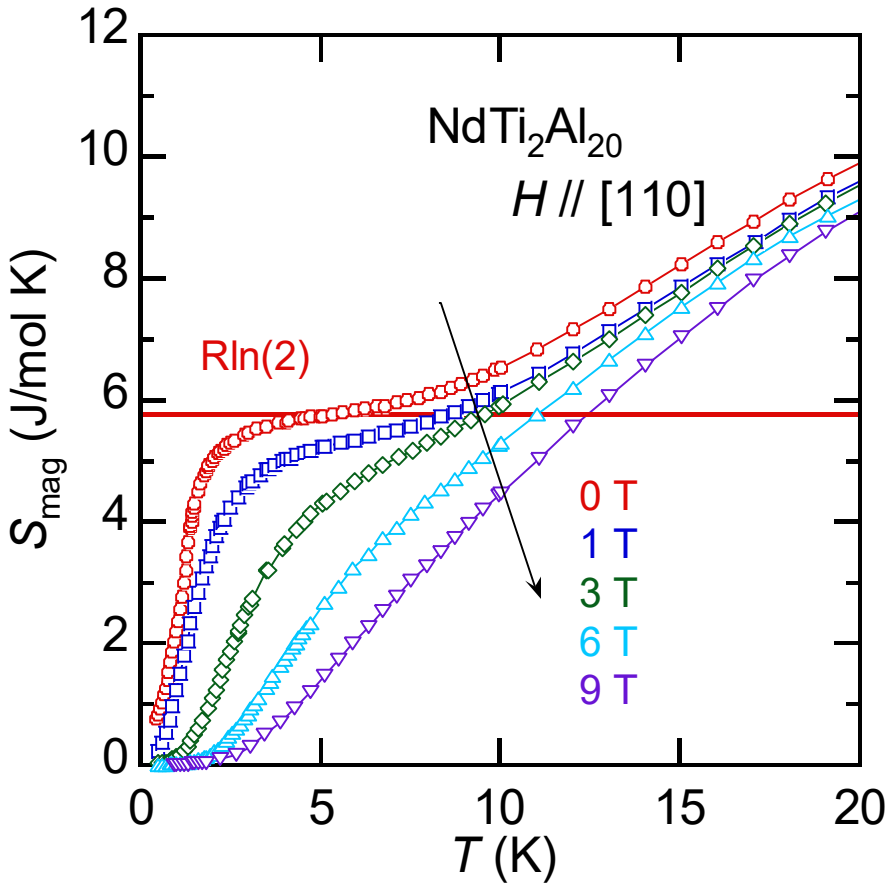

Figure 4.5: Temperature dependences of the magnetic entropy S_{mag} for $NdTi_2Al_{20}$ in various applied magnetic fields along the [110] direction.

entropy below 0.5 K was obtained by $S_{mag} = \int_0^{0.5} \frac{C_{mag}}{T} dT$, where the values of C_{mag} / T below 0.5 K were estimated by linearly extrapolating the data between 0.5 and 1.0 K to 0 K. The estimated magnetic entropy below 0.5 K for zero field was about 0.7 J/(mol·K), while

the S_{mag} values below 0.5 K for 1 – 9 T are negligible. In zero field, the magnetic entropy S_{mag} grows rapidly with increasing temperature and reaches the value of R ln 2 [5.76 J/mol·K] around 5 K where it manifests a noticeable change of slope. The specific heat measurements for [100] and [111] directions were also carried out (data not shown), and no anisotropy was observed at low temperatures and small fields. These results as well as the field dependences of magnetization along the three principal crystallographic axes suggest an isotropic Γ_6 doublet rather than an anisotropic Γ_8 ground state for $NdTi_2Al_{20}$.

4.1.3. Electrical resistivity

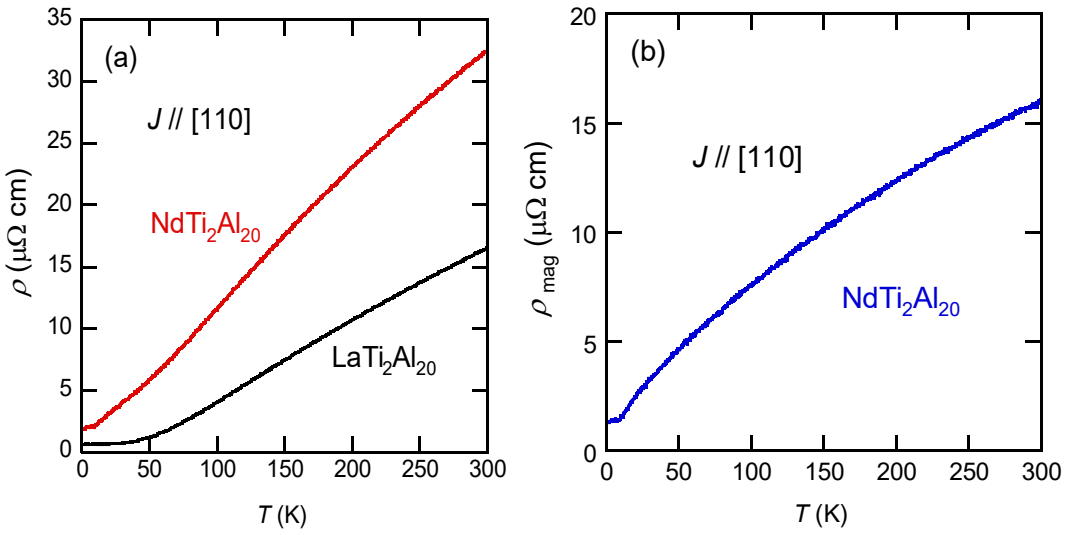

Figure 4.6: Temperature dependences of (a) electrical resistivities for $NdTi_2Al_{20}$ and $LaTi_2Al_{20}$ single crystals, (b) magnetic part of electrical resistivity for $NdTi_2Al_{20}$ with the current J along the [110] direction in zero field.

Figure 4.6(a) displays the resistivities for single crystals of $NdTi_2Al_{20}$ and $LaTi_2Al_{20}$ with the current J along the [110] direction in zero field. The residual resistivity ratios, defined as

RRR = ρ(300 K) / ρ(1.9 K), for $NdTi_2Al_{20}$ and $LaTi_2Al_{20}$ are about 17 and 26, respectively, indicating good qualities of the as-prepared single crystals. The resistivities of $NdTi_2Al_{20}$ and $LaTi_2Al_{20}$ increase with increasing temperature, and no anomaly was found in the temperature range from 1.9 to 300 K. The magnetic part of the resistivity ρ_{mag} for $NdTi_2Al_{20}$ was obtained by $\rho_{mag} = \rho(NdTi_2Al_{20}) - \rho(LaTi_2Al_{20})$, as shown in Figure 4.6(b). ρ_{mag} is almost a constant below 10 K and increases with increasing temperature above 10 K. The curvature of $\rho_{mag}(T)$ curve changes with increasing temperature, suggesting the presence of CEF effect.

4.2. Analyses and discussion

Since Nd^{3+} ($4f^3$) is a Kramers ion with an odd number of electrons, the doublet degeneracy is protected and cannot be lifted in each level without applied field. As can be seen from Figure 2.3, there are only Γ_6 doublet and Γ_8 quartet for Nd^{3+} in the cubic symmetry. In this section, CEF effects are discussed based on the experimental results of magnetizations and specific heats.

The change of slope in magnetic entropy around 5 K where $S_{mag}(T) = R \ln 2$ suggests a doublet ground state in $NdTi_2Al_{20}$. The Γ_6 doublet is magnetically isotropic and Γ_8 quartet is anisotropic in fields. The almost isotropic behavior in magnetizations and specific heats at low temperatures origin in the isotropic Γ_6 doublet ground state. The magnetic and thermal properties are discussed using the following Hamiltonian including a CEF term, a Zeeman term, and an exchange term:

$$\mathcal{H}_i = W\left(x\frac{O_4}{F(4)} + (1-|x|)\frac{O_6}{F(6)}\right) + g_J\mu_B \boldsymbol{J}_i \boldsymbol{H}_{\text{ext}} + g_J\mu_B \boldsymbol{J}_i \boldsymbol{H}_{\text{mol}}(i), \tag{4.1}$$

where *i* is for sublattices A with up magnetic moments or sublattices B with down magnetic moments in antiferromagnetic structure, $\boldsymbol{H}_{\text{ext}}$ and $\boldsymbol{H}_{\text{mol}}$ are external magnetic field and molecular field, respectively. The second and third terms of Equation (4.1) are the Zeeman energy and the exchange energy. The molecular field $\boldsymbol{H}_{\text{mol}}(i)$ at the *i* sublattice can be written as $n_{BA}(g_J\mu_B)\langle \boldsymbol{J}_j \rangle$, where $\langle \boldsymbol{J}_j \rangle$ is the thermal average in the other sublattices *j*, $n_{BA}$is the exchange parameter between atoms in A and B sublattices. The magnetization for each sublattice is

$$\boldsymbol{M}_i = -g_J\mu_B\langle \boldsymbol{J}_i \rangle = -g_J\mu_B \frac{Tr\boldsymbol{J}_i \exp(-\beta\mathcal{H}_i)}{Tr\exp(-\beta\mathcal{H}_i)}, \tag{4.2}$$

where $\beta = 1/k_BT$. The average magnetization $\boldsymbol{M} = (\boldsymbol{M}_{\text{A}} + \boldsymbol{M}_{\text{B}})/2$. Since $\boldsymbol{H}_{\text{ext}}$, $\boldsymbol{H}_{\text{mol}}$ and $\boldsymbol{J}_i$ are three-dimensional vectors, Equation (4.2) is a set of six equations about the *x*-, *y*-, *z*-components of $\boldsymbol{M}_{\text{A}}$ and $\boldsymbol{M}_{\text{B}}$, and is solved by the iteration method. The molar specific heat

$$C = \left(\frac{N_A}{2}\right)\frac{\partial}{\partial T}\left(\langle \mathcal{H}_{\text{A}} \rangle + \langle \mathcal{H}_{\text{B}} \rangle - \frac{1}{2}\langle \mathcal{H}_{\text{exch}} \rangle\right) \tag{4.3}$$

We have three parameters, i.e., the energy scale *W*, *x*, and the exchange parameters n_{BA} for numerical calculations to fit the experimental results in the previous section. According to the energy scheme of Nd^{3+} ion, as shown in Figure 2.3, the ground state is Γ_6 is $W > 0$ and $-1 \le x \le 0.37$, or $W < 0$ and $0.83 \le x \le 1$. With the experimental results of magnetizations $M(T, H)$ and specific heats $C(T, H)$, *W* and *x* were determined to be 6 K and 0.3 respectively. *W* and *x* were scanned during this process over large scale without considering the exchange interactions. The parameter *x* was chosen between − 1 and 1 with a step of 0.05 and additional

values of x were also used when necessary. Then the values of n_{BA} were adjusted in a step a 0.01 to fit the experimental results of magnetizations and specific heats, and the appropriate values of n_{BA} were determined to be − 0.4, respectively.

The calculated temperature dependences of M / H, and the inverse susceptibility H / M are displayed in Figure 4.7(a) and Figure 4.7(b), respectively. The overall temperature dependent behaviors were reproduced qualitative: the Néel temperature T_N = 1.4 K and a deviation from the linear fitting at low temperatures. However, the M / H value at T_N is only 40% that of the experimental one.

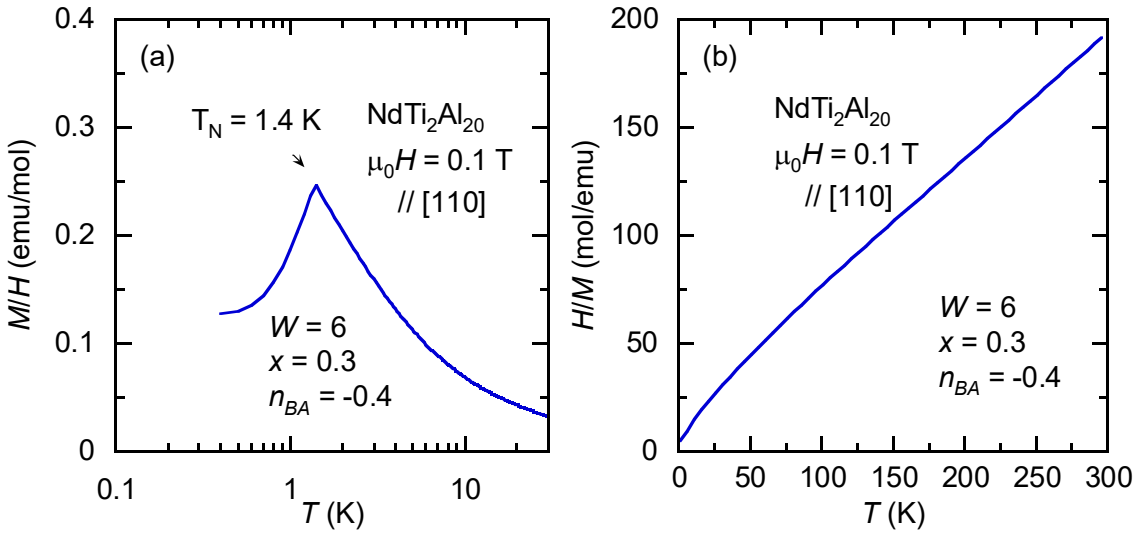

Figure 4.7: Calculated temperature dependences of (a) the magnetic susceptibility M / H on a logarithmic temperature scale, and (b) the inverse magnetic susceptibility H / M for $NdTi_2Al_{20}$ in an applied field of 0.1T along the [110] direction.

Figure 4.8(a) shows the calculated field dependences of magnetization at various constant temperatures in applied magnetic fields along [110]. The value of magnetization at 7 T for

each temperature agrees well with the experimental results. However, the magnetization at 0.5 K shows saturation tendency in an applied field of about 3 T rather than 1 T as observed in experimental result. A metamagnetic transition was also observed at 0.5 K, as shown in Figure 4.8(b).

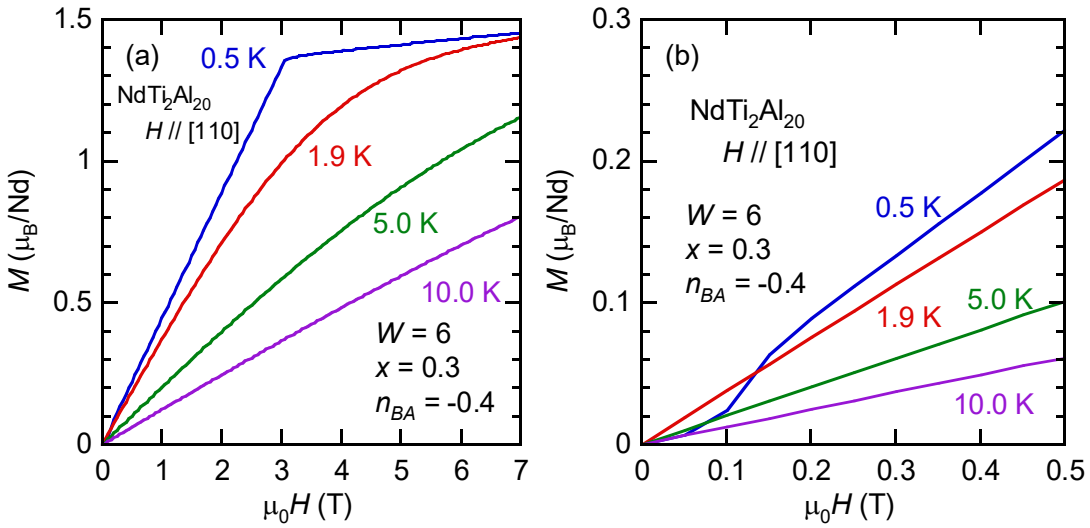

Figure 4.8: Calculated field dependences of magnetization at various constant temperatures (a) in applied magnetic fields along [110] up to 7 T, and (b) below 0.5 T.

Figure 4.9(a) and Figure 4.9(b) display the calculated temperature dependences of the magnetic specific heat in the form of C_{mag} / T and magnetic entropy S_{mag} for $NdTi_2Al_{20}$ in various applied magnetic fields along the [110] direction, respectively. The calculated specific heat in zero field was reproduced qualitatively with the peak near T_N, although the peak value is almost twice that of the experimental one. The calculated magnetic specific heat in the form of C_{mag} / T at 1 T almost overlaps that at zero field and the peak position and value of C_{mag} / T at 3 T show great difference with the experimental results.

As can be seen, the inconsistences between the calculated and experimental results occur at low temperature near T_N rather than much higher temperature, which might be attributed to the fact that the calculations is based on the molecular-field approximation without considering the magnetic fluctuation$(J_A - \langle J_A \rangle)(J_B - \langle J_B \rangle)$. The magnetic fluctuation plays a more important role near T_N than at temperatures far away from T_N. The interaction between the A sublattices was not taken into consideration, which might also lead to the differences between calculated and experimental results. Extensive calculations considering the interaction between the A sublattices were carried out, but no satisfactory results have been obtained for the moment.

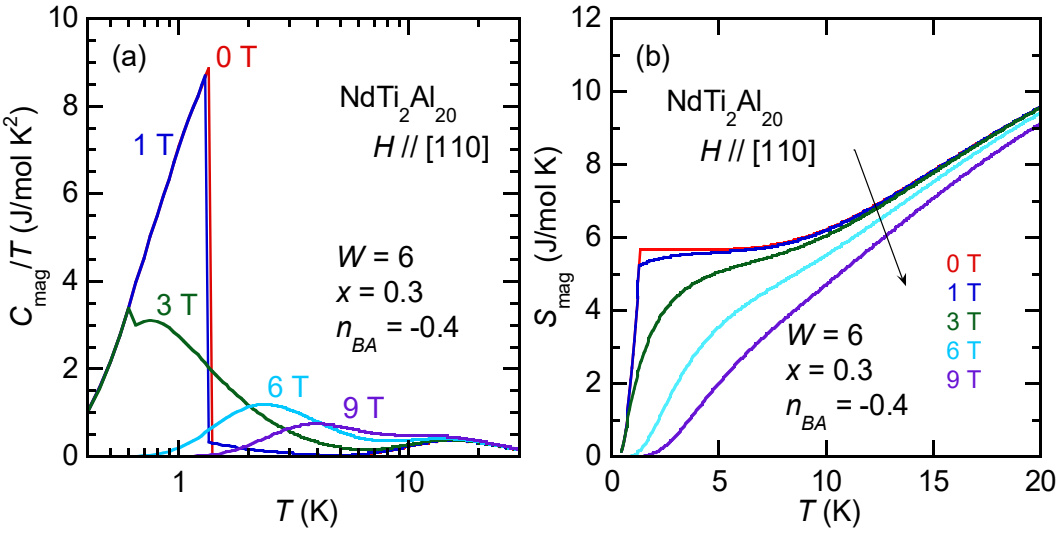

Figure 4.9: Calculated temperature dependences of (a) the magnetic specific heat in the form of C_{mag} / T, and (b) magnetic entropy S_{mag} for $NdTi_2Al_{20}$ in various applied magnetic fields along the [110] direction.

The magnetic entropies S_{mag} for $NdTi_2Al_{20}$ in fields along the [110] direction were well produced with the parameters $W = 6$, $x = 0.3$, and $n_{BA} = -0.4$. The corresponding CEF scheme

is Γ_6 – (0 K, doublet) – $\Gamma_8^{(1)}$ (53 K, quartet) – $\Gamma_8^{(2)}$ (443 K, quartet). The CEF splitting of 53 K between the ground state and the first excited state is in good agreement with the experimental result of temperature dependent magnetization as shown in Figure 4.1(b).

4.3. Conclusion

Single crystals of $NdTi_2Al_{20}$ and $LaTi_2Al_{20}$ were grown with the Al self-flux method. $NdTi_2Al_{20}$ was found to be antiferromagnetic with the Néel temperature T_N = 1.4 K, the effective magnetic moment μ_{eff} = 3.56 μ_B (Nd^{3+}: 3.64 μ_B), and the Curie-Weiss temperature θ_P = –28.50 K. The effective magnetic moment μ_{eff} = 3.56 μ_B is close to that of the free Nd^{3+}, indicating the localized nature of 4*f* electrons in $NdTi_2Al_{20}$. Metamagnetic transitions were observed at 0.5 K in applied field around 0.16 T along the principal axes [100], [110], and [111].

Specific heats of the single crystals of $NdTi_2Al_{20}$ were measured in applied fields up to 9 T in the temperature range from 0.5 to 300 K with the isostructural single crystals of $LaTi_2Al_{20}$ as the nonmagnetic reference. The peak of the specific heat for $NdTi_2Al_{20}$ shifts to lower temperature region with increasing applied field below 1 T, which is a typical behavior of the AFM ordering compounds. While in applied fields above 1 T, the peak of specific heat shifts to higher temperature region and becomes broader with increasing applied field, showing the Schottky-like anomaly. The magnetic entropy S_{mag} grows rapidly with increasing temperature and reaches the value of R ln 2 around 5 K in zero field. The resistivity of $NdTi_2Al_{20}$ increases with increasing temperature, and no anomaly was found in the

temperature range 1.9 – 300 K. A Γ_6 doublet ground state of the Nd^{3+} ion is suggested by these results.

The experimental results of magnetizations M (T, H) and specific heats C(T, H) were analyzed by theoretical calculations, and a CEF scheme Γ_6 – (0 K, doublet) – $\Gamma_8^{(1)}$ (53 K, quartet) – $\Gamma_8^{(2)}$ (443 K, quartet) was proposed with the CEF parameters W = 6 K, x = 0.3, and n_{BA}= − 0.4. The inconsistences between the calculation results and experimental results of magnetizations and specific heats were observed near T_N, which might be attributed to the fact that the magnetic fluctuation $(J_A - \langle J_A \rangle)(J_B - \langle J_B \rangle)$ and exchange interaction between A sublattices was not taken into account.

5. Possible heavy fermion state of the caged cubic compound NdV_2Al_{20}

5.1. Experimental results

5.1.1. Magnetic properties

The temperature dependences of magnetization *M* along the three principal axes [100], [110], and [111] in an applied field of 0.1 T and in a smaller field of 0.01 T along the [100] direction are shown in Figure 5.1(a). The rapid increase of magnetization in 0.01 T indicates a ferromagnetic (FM) phase transition with a Curie temperature around 1.8 K. Figure 5.1(b) shows the temperature dependence of inverse susceptibility *H* / *M*, manifesting considerable curvature at high temperatures which is different from that of $NdRu_2Zn_{20}$ with a linear behavior [6]. The Pauli paramagnetic-like contribution is not negligible and it does not obey the simple Curie-Weiss law $\chi = \frac{M}{H} = \frac{N\mu_{eff}^2}{3k_B(T-\theta_p)}$. But it could be well fitted to the modified Curie-Weiss law, which is in the form $\chi = \frac{M}{H} = \frac{N\mu_{eff}^2}{3k_B(T-\theta_p)} + \chi_0$, above 50 K. The effective moment μ_{eff}, the Curie-Weiss temperature θ_P and the temperature-independent part of the magnetic susceptibility χ_0 for NdV_2Al_{20} are estimated to be $2.95\mu_B$, 3.3 K and 1.1×10^{-3} emu/mol, respectively. The observed value of effective magnetic moment μ_{eff} is much smaller compared to that of the free Nd^{3+} ion ($3.62\ \mu_B$), which might due to the CEF effect and the strong *c-f* hybridization. The positive sign of θ_P suggests a ferromagnetic correlation

between the Nd^{3+} ions. The obtained χ_0 is about an order of magnitude larger than the experimental value of LaV_2Al_{20} with the opposite sign. [12,114]

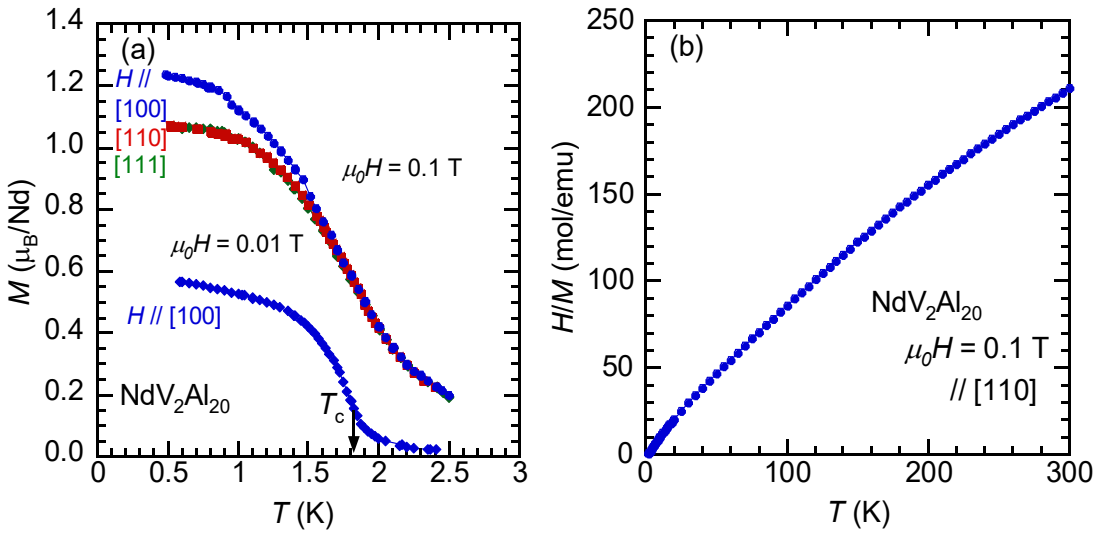

Figure 5.1: (a) Temperature dependences of magnetization M of NdV_2Al_{20} in an applied magnetic field of 0.1 T along the three principal axes and in a field of 0.01 T along the [100] direction. (b) The temperature dependence of the inverse magnetic susceptibility H / M in a field of 0.1 T along the [100] direction.

Figure 5.2(a) shows the field dependences of magnetization M along the [100] direction up to 7 T at some constant temperatures. At low temperature of 0.5 K, M increases sharply with increasing applied field below 0.5 T, then shows a saturation tendency in high fields. At temperatures above 2 K, the magnetizations increase gradually with increase in applied fields. Figure 5.2(b) shows the field dependences of M in the magnetic fields along the three principal axes up to 7 T at 0.5 K. A clear anisotropy was observed above 2 T. The [110] and [111] axes are easy and hard axes of magnetization, respectively. The ferromagnetic moments at 0.5 K obtained by extrapolating the high field data to 0 T, are approximately 1.4

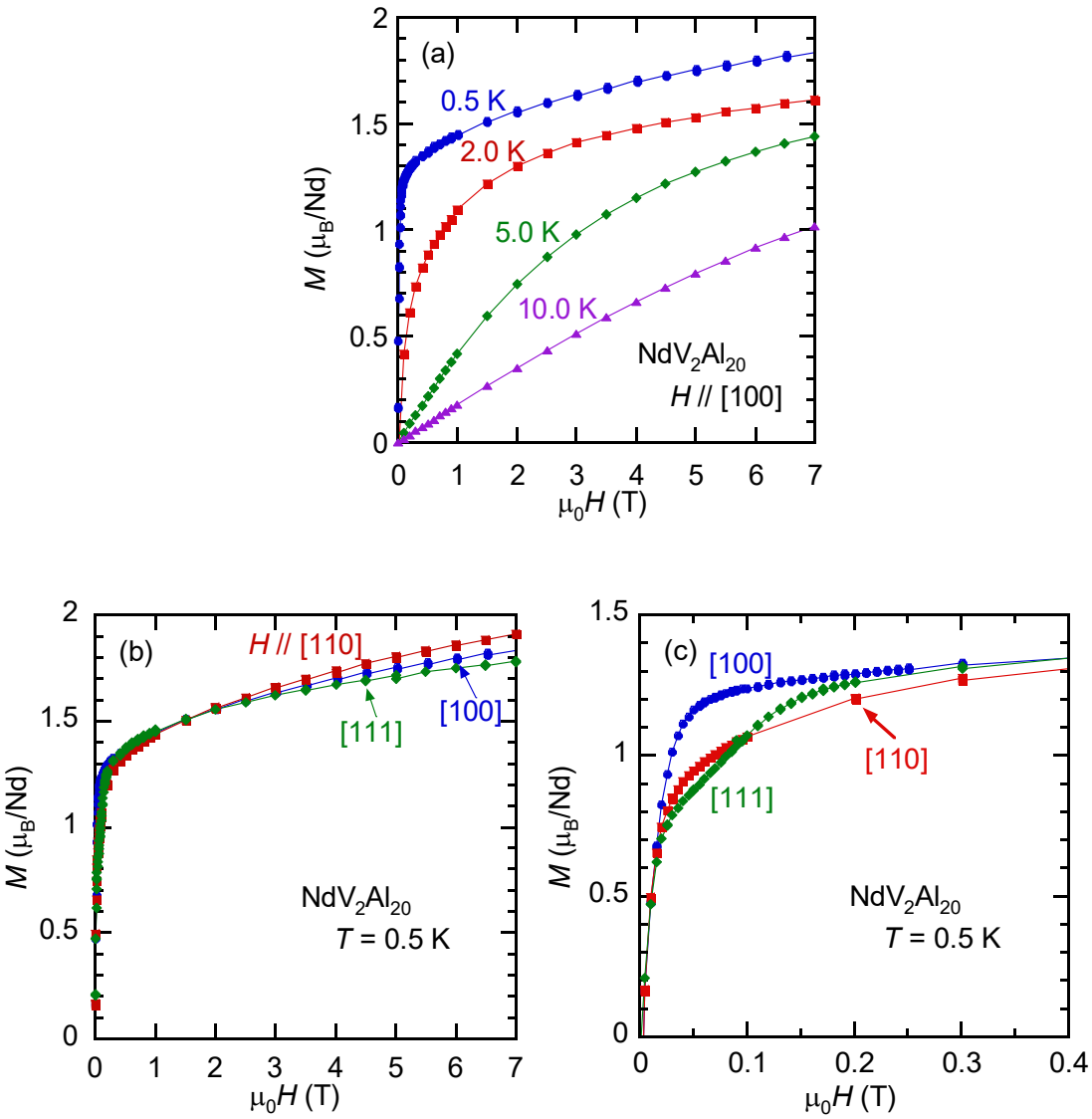

Figure 5.2: (a) Magnetization curves of NdV_2Al_{20} in magnetic fields along the [100] direction. (b) Magnetization curves of NdV_2Al_{20} in magnetic fields along the three principal crystallographic axes at 0.5 K. (c) Magnetization curves below 0.4 T.

μ_B/Nd for all the three principal axes, which is less than half that of the Nd^{3+} (3.28 μ_B). This considerable reduction of the moments can be attributed to the CEF effect. Figure 5.2(c)

shows the field dependences of M at 0.5 K in low fields below 0.4 T. It is evident from Figure 5.2(c) that the easy axis of magnetization changes from the [110] axis above 2 T to the [100] axis in low fields. In the [100] and [110] directions, M increases steeply near zero fields, and tends to saturate at around 0.2 T. In the [111] direction, M increases steeply near zero field, then increases linearly up to about 0.15 T and shows a saturation tendency. Similar behaviors were also observed in $NdRu_2Zn_{20}$. [6] In low fields, the easy axis of magnetization is [100]. There is little hysteresis in the observed M (H) curves. The M values obtained by extrapolating high field data smoothly to 0 T (M_0) are approximately 1.2, 0.9, and 0.7 μ_B/Nd for the [100], [110], and [111] directions, respectively. The ratio of these values is about $1:\sqrt{1/2}:\sqrt{1/3}$, which indicates that the M_0 values for the [110] and [111] directions are the projections of the M_0 value of the [100] direction.

5.1.2. Specific heat and magnetic entropy

Figure 5.3(a) shows the temperature dependences of specific heat for NdV_2Al_{20} in various fields along the [100] direction. The specific heat of the nonmagnetic isostructural single crystal LaV_2Al_{20} was also measured to estimate the electron and phonon contributions to the specific heat. As can be seen from Figure 5.3(a), specific heat C for LaV_2Al_{20} decreases monotonically with decreasing temperature from 20 to 1.9 K. With a C / T vs T^2 plot, the electronic specific heat coefficient γ and the Debye temperature Θ_D were estimated to be 21 mJ/(mol·K^2) and 527 K, respectively, which are close to the values in a previous report. [114] A sharp λ-type anomaly was observed near 1.8 K in the zero field specific heat of NdV_2Al_{20}, which indicates a magnetic phase transition and is in good agreement with the Curie

temperature observed in the magnetization measurement as shown in Figure 5.1(a) and our previous report [7]. The λ-type peak changes to round peaks when external fields are applied and shifts to higher temperature with increasing fields.

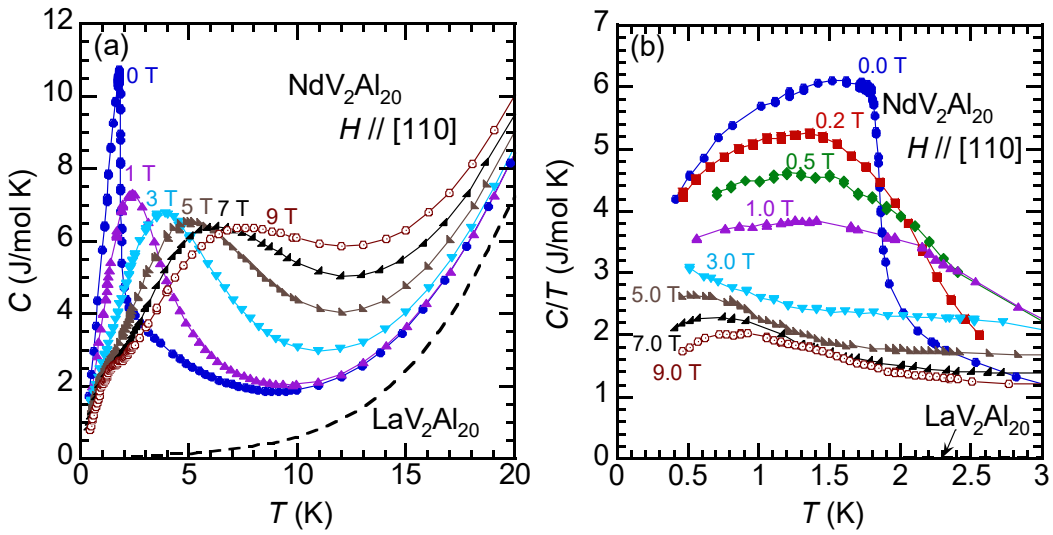

Figure 5.3: (a) Temperature dependences of the specific heat C for NdV_2Al_{20} in various fields along the [100] direction. The dashed line is the temperature dependence of C for LaV_2Al_{20}. (b) The temperature dependences of the specific heat divided by temperature C / T for NdV_2Al_{20} and LaV_2Al_{20}.

Figure 5.3 (b) shows the temperature dependences of the specific heat divided by temperature C / T in low temperature region below 3 K. The C / T of NdV_2Al_{20} in zero field below T_C decreases with decreasing temperature, and an extremely large value of about 4 J/(mol·K^2) remains at 0.5 K. The γ value of NdV_2Al_{20}, which is estimated from an extrapolation of the C / T data in zero field to 0 K, is about 2 J/(mol·K^2). This γ value is large even compared to the possible Nd-based heavy fermion compound $NdOs_4Sb_{12}$. [92,115] The

large C / T remains in high magnetic fields, and the observed C / T is more than 1J/(mol·K^2) in 9 T below 3 K. These results imply that NdV_2Al_{20} is a possible heavy fermion compound.

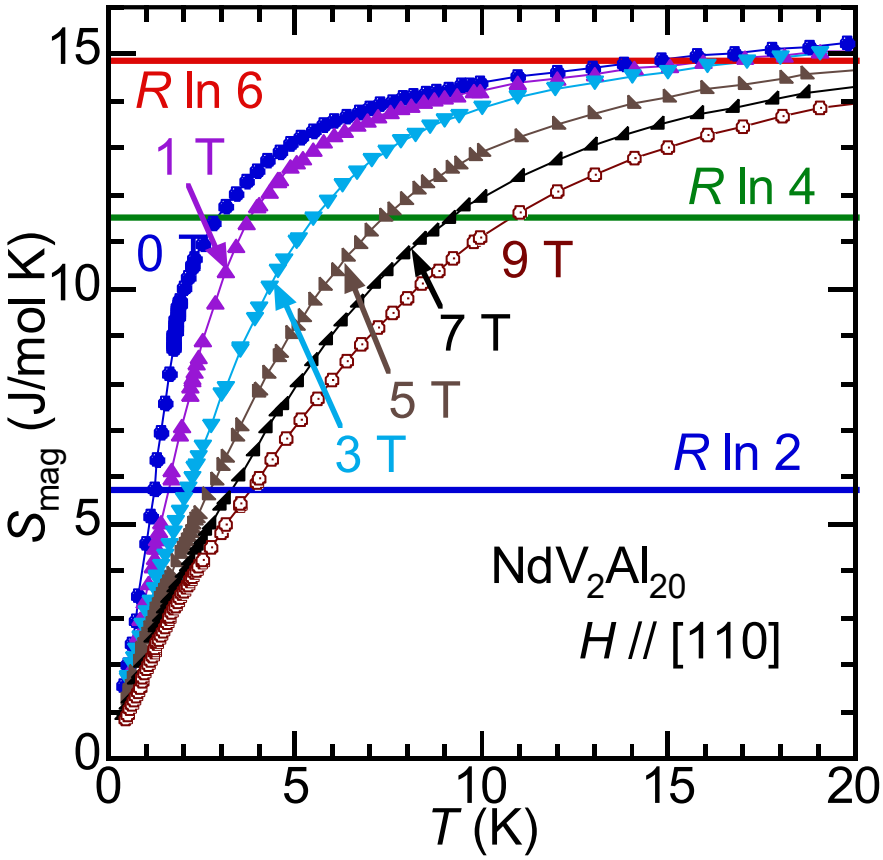

Figure 5.4: Temperature dependences of the magnetic part of the entropy S_{mag} for NdV_2Al_{20} in various fields along the [100] direction.

Figure 5.4 shows the magnetic part of the entropy S_{mag} of NdV_2Al_{20} in various fields. The obtained S_{mag} in zero field increases sharply with increasing temperature up to R ln 4 near T_C and the gradually increases up to R ln 6 near 20 K. In external magnetic fields up to 9 T, S_{mag} show similar behaviors with lower increasing rates. The results suggest that the ground state

of Nd^{3+} ion is a quartet state and the first excited state of a doublet locates about 20 K above the ground state.

5.1.3. Electrical resistivity

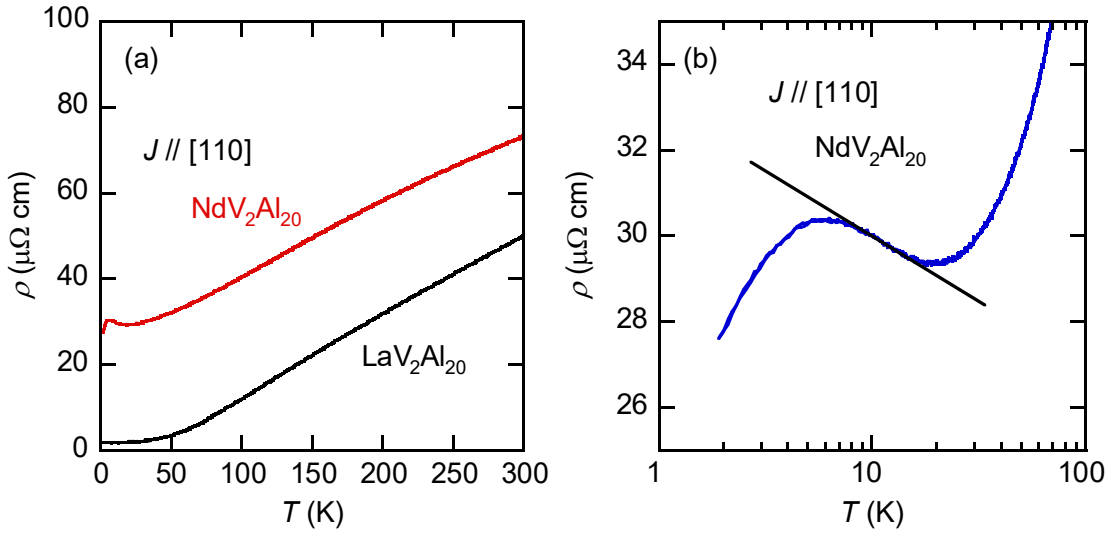

Figure 5.5: (a) Temperature dependences of electrical resistivity ρ for single crystals of NdV_2Al_{20} and polycrystalline LaV_2Al_{20} with the current J along the [110] direction in zero field. (b) The temperature dependence of electrical resistivity ρ for NdV_2Al_{20} on a logarithmic temperature scale.

Figure 5.5(a) shows the temperature dependences of electrical resistivity ρ for single crystals of NdV_2Al_{20} and polycrystalline LaV_2Al_{20} with the current J along the [110] direction in zero field. The electrical resistivity for NdV_2Al_{20} and LaV_2Al_{20} monotonically increase above 20 K and 2 K, respectively, with no observable anomaly. The residual resistivity ratios RRR, defined as ρ(300 K)/ρ(2 K), for NdV_2Al_{20} and LaV_2Al_{20} are about 3 and 25, respectively. Figure 5.5(b) shows the electrical resistivity ρ for NdV_2Al_{20} on a

logarithmic temperature. It is evident from Figure 5.5(b) that ρ for NdV_2Al_{20} takes a minimum near 20 K, then shows a $-\log T$ increase with decreasing temperature and makes a peak at around 5 K, which is a typical behavior in Kondo compounds.

5.2. Analyses and discussion

We attempted to explain the experimental results of magnetization and specific heat of NdV_2Al_{20} by taking into account the CEF effect with the same procedures in the literature [6,116], using the CEF parameters of W and x given by Lea *et al.* for the CEF energy schemes (LLW) [104]. Theoretically the energy levels of Nd^{3+} in CEF are determined by the parameters W and x. [104] In the calculation process we referred to the LLW energy scheme of the Nd^{3+} ion as a function of x when $W = 1$ in cubic symmetry CEF which is shown in Figure 2.3.

The easy direction and the calculated M are shown in Figure 5.6(a) and Figure 5.6 (b). If we take a priority on the observed magnetic entropy of $R \ln 4$ near T_C, i.e., the energy scheme of quartet ground state and doublet excited state, possible regions of W and x are (1) $W > 0$, $0.4 < x < 0.8$, and (2) $W < 0$, $0.4 < x < 0.8$. The calculated magnetizations of Nd in these regions, however, are more than 2 μ_B as seen in the figures, which is inconsistent with the observed magnetization, $1.4\mu_B$, as shown in Figure 5.2(a). If we take a priority on the magnetization and magnetic anisotropy, i.e., 1.3 μ_B/Nd and the easy direction of [100] at 0.5 K, possible regions for the fitting parameters W and x are (1) $W > 0$, $-1 \leq x < -0.4$, (2) $W < 0$, $0.8 < x \leq 1$, and (3) $W < 0$, $x \simeq -0.45$. However, the energy scheme of the ground state and

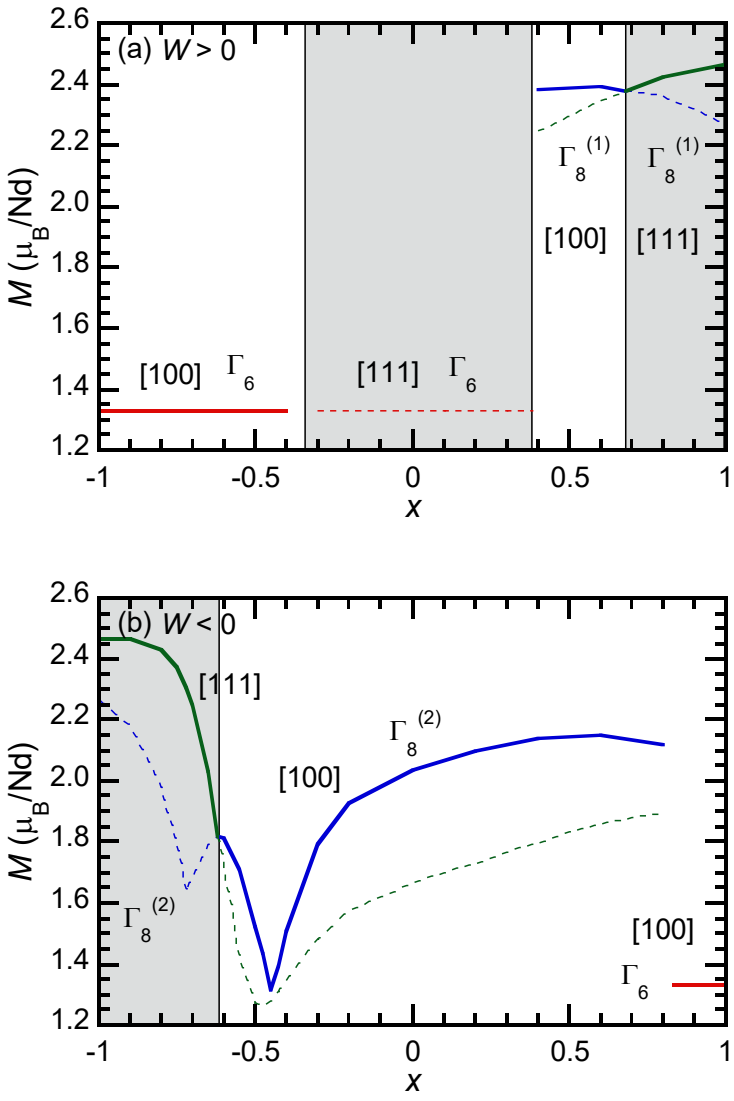

Figure 5.6: Calculated magnetizations of Nd^{3+} ion in a cubic symmetry site as functions of the CEF parameters W and x, when (a) $W > 0, -1 \leq x \leq 1$, (b) $W < 0, \ -1 \leq x \leq 1$. The calculated magnetizations are independent of W. The regions of the x parameter with larger magnetizations (solid lines), are selected.

the first excited state in the former two cases are doublet-quartet state and in the third case is the quartet-quartet. These energy schemes conflict with the deduced energy scheme from the magnetic entropies. Consequently, it is concluded that the present experimental results

cannot be consistently explained by the present calculations. Further extensive CEF calculations were made taking the Zeeman effect and the exchange interaction into consideration, but no appropriate W and x values could be obtained for the moment.

The filled skutterudite compound $NdOs_4Sb_{12}$ [19,91,92,115], which is also in a FM state has revealed a large γ value and possible heavy-fermion behavior based on the specific heat measurements. The logarithmic temperature dependence of ρ and a large C / T were observed in the heavy fermion compound PrV_2Al_{20} and $PrFe_4P_{14}$ above the quadrupolar ordered temperature. [2,117] The behaviors of logarithmic temperature dependence of ρ and large values of C/T are similar to those observed in NdV_2Al_{20}. The observed physical properties for magnetizations, specific heats, and electrical resistivities indicate a possible heavy fermion state of NdV_2Al_{20}.

5.3. Conclusion

Single crystals of NdV_2Al_{20} were made by Al self-flux method. Physical properties of NdV_2Al_{20} single crystals were investigated by means of magnetization, specific heat and electrical resistivity measurements in wide temperature range in applied magnetic fields along the principal axes. Polycrystalline LaV_2Al_{20} were used as the nonmagnetic reference. A ferromagnetic (FM) phase transition was observed at the Curie temperature T_C = 1.8 K in both magnetization and specific heat measurements. The field dependence of M shows an anisotropy at 0.5 K with the easy direction of magnetization along [100] below 0.2 T. And the easy direction changes from the [100] direction in low fields to the [110] direction above 2 T.

On cooling below 2 K in zero field, the specific heat divided by temperature C / T shows an enhanced value with a large electronic specific heat coefficient γ of about 2 J/(mol·K^2). The large C / T value of more than 1 J/(mol·K^2) remains in a high field of 9 T below T_C.The electrical resistivity for NdV_2Al_{20} shows a logarithmic temperature dependence at around 10 K. The magnetic entropies S_{mag} are R ln 4 near the Curie temperature T_C and reach R ln 6 near 20 K, suggesting a quartet ground state and a doublet first excited state.

The CEF calculations for energy scheme were carried out, which were found to be unable to explain the observed M and S_{mag} consistently for the moment. These results suggest a heavy fermion state for NdV_2Al_{20}.

6. Magnetic and thermal properties of TmV_2Al_{20}

6.1. Experimental results

6.1.1. Magnetic properties

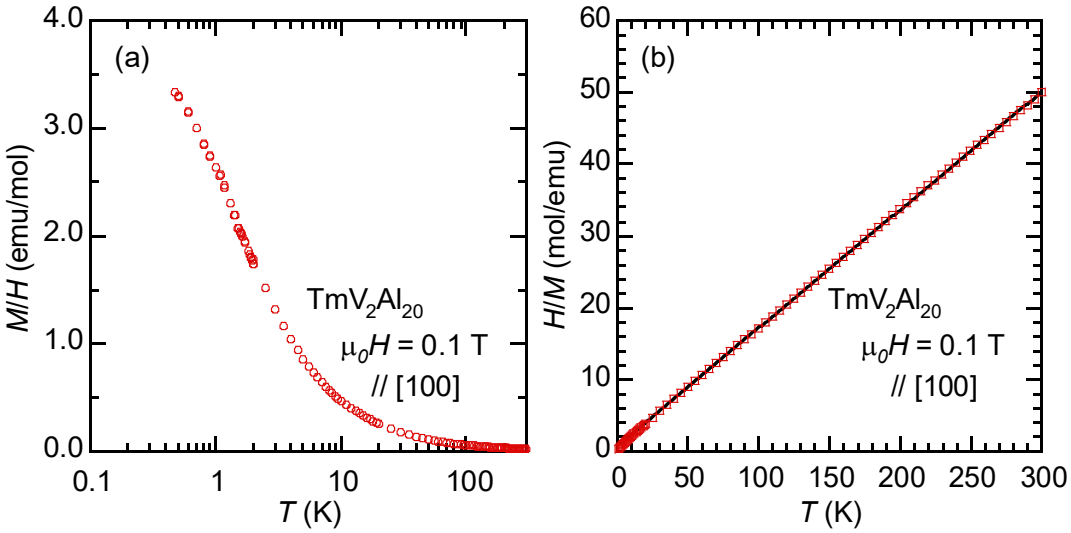

Figure 6.1: (a) Temperature dependence of the susceptibility M / H for TmV_2Al_{20} measured in an applied magnetic field of 0.1 T along [100] axis on a logarithmic temperature scale. (b) Temperature dependence of the inverse susceptibility H / M for TmV_2Al_{20} in a field of 0.1 T along [100] axis, the solid line represents the Curie-Weiss fitting between 50 and 300 K.

The temperature dependence of magnetization (M) for TmV_2Al_{20} was measured in an external magnetic field (H) of 0.1 T along the [100] direction down to 0.5 K. Figure 6.1(a) shows the temperature dependence of the M / H for TmV_2Al_{20} measured in an applied magnetic field of 0.1 T along [100] axis on a logarithmic temperature scale, the susceptibility

M / H shows a –log T dependence increase with decreasing temperature below 5 K. The obtained H / M data are shown in Figure 6.1(b). A linear fit of the H / M data above 50 K yields the paramagnetic Curie temperature, $\theta_P = -5$ K, and the effective magnetic moment, $\mu_{eff} = 7.0\ \mu_B$, which is close to that of the free Tm^{3+} ion (7.57 μ_B). As shown in Figure 6.1(a), there is no noticeable magnetic phase transition in the M / H curve. TmV_2Al_{20} is paramagnetic above 0.5 K, which implies that the ground state is the nonmagnetic singlet (Γ_1, Γ_2) or doublet (Γ_3) state.

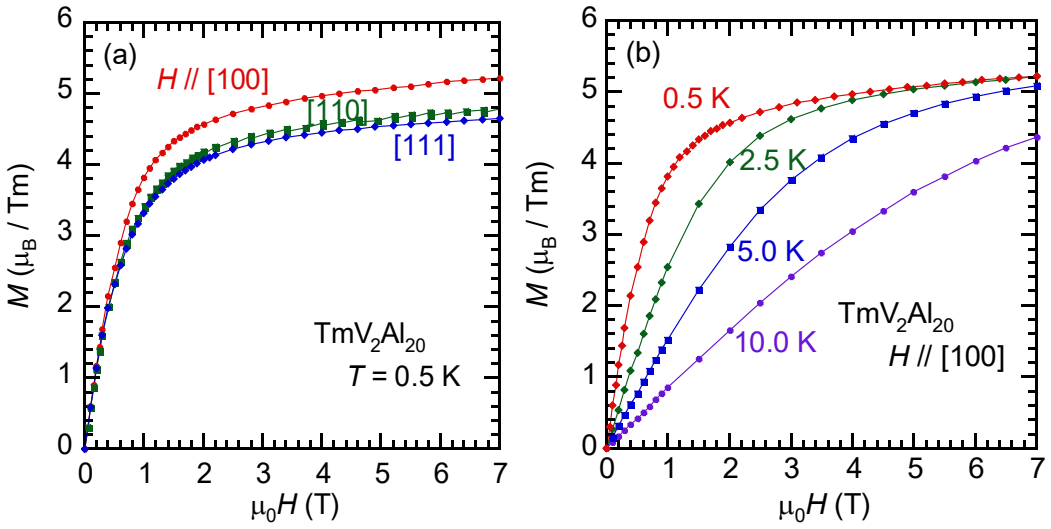

Figure 6.2: Magnetization curves of TmV_2Al_{20} in the magnetic field up to 7 T (a) along the principal crystallographic axes [100], [110] and [111] at 0.5 K, (b) along the [100] direction at various temperatures.

The field dependences of magnetization M (H) were measured in external fields up to 7 T. Figure 6.2(a) shows M (H) curves in the field along the principle axes, [100], [110], and [111] at 0.5 K. The M values were found to be zero at $\mu_0 H = 0$ T, and gradually increased with increasing field. No magnetic hysteresis was noticed on the M (H) curves. It is clear that

the magnetically easy axis is along the [100] direction, and the hard axis is along the [111] direction. Sets of the M (H) data were acquired in the field along the easy [100] direction at constant temperatures of 0.5, 2.5, 5.0 and 10 K, as shown in Figure 6.2(b). The M value at $\mu_0 H = 7$ T and $T = 0.5$ K is 5.2 μ_B/Tm, which is approximately three-fourths of the saturation magnetization for the free Tm^{3+} ion (7.0 μ_B). The similar result has been reported in the case of $TmTi_2Al_{20}$ that the magnetization at $\mu_0 H = 7$ T and $T = 2$ K is 5 μ_B/Tm in Ref. [90]. The reduction of magnetization is most likely due to the CEF effect, which will be discussed in the next section.

6.1.2. Specific heat and magnetic entropy

The temperature dependences of the specific heat were measured with external fields along the [100] direction down to 0.5 K ($\mu_0 H = 0 – 6$ T) or 2.0 K ($\mu_0 H = 9$ T). Figure 6.3(a) shows low-temperature part of the observed specific heats, in which the peaks become broadened and shift to higher temperatures with increasing external field, indicating the Schottky anomaly. The electron and phonon contributions to the specific heat were estimated using the observed specific heat of LuV_2Al_{20} (dashed line in Figure 6.3(a)). The magnetic part of the specific heat of TmV_2Al_{20} were evaluated by subtracting the specific heat data of LuV_2Al_{20} from those of TmV_2Al_{20}, i.e., $C_{mag} = C(TmV_2Al_{20}) – C(LuV_2Al_{20})$. The resultant C_{mag} / T vs T curves were plotted in Figure 6.3(b) on a logarithmic temperature scale and in Figure 6.3(c) on a linear temperature scale.

The observed C_{mag} / T at 0 T show the –log T dependence at low temperatures, which is similar to the M / H curve. Furthermore, the C_{mag}/T value at 0 T and 0.6 K is approximately

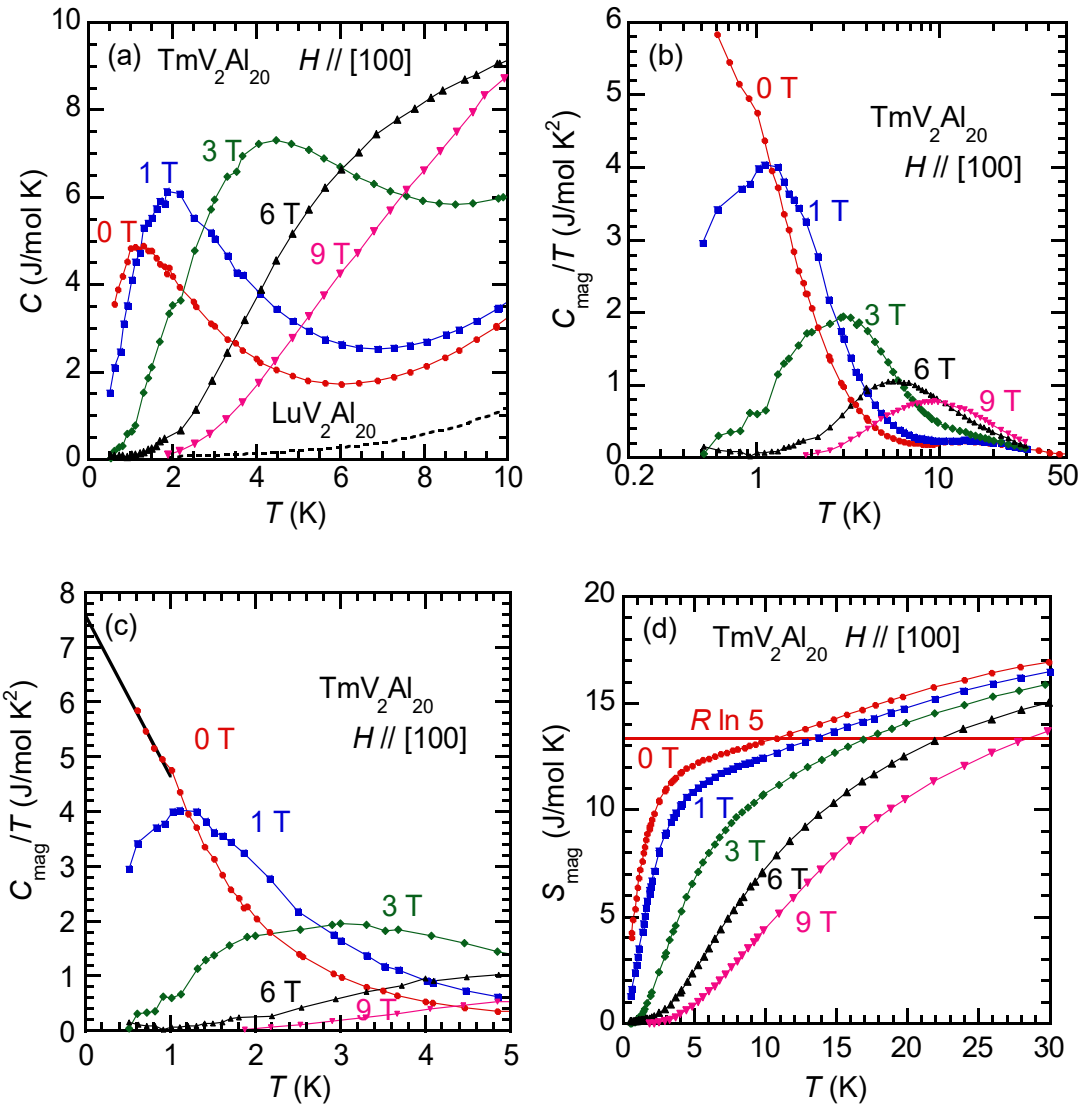

Figure 6.3: (a) Temperature dependences of the specific heat C for TmV_2Al_{20} at various H along the [100] direction, the dashed line is the temperature dependence of the specific heat for LuV_2Al_{20}. Temperature dependences of C_{mag} / T for TmV_2Al_{20} in various magnetic fields along the [100] direction (b) on a logarithmic temperature scale, and (c) on a linear temperature scale, the solid line is a linear extrapolation of the data between 0.5 and 1.0 K to 0 K. (d) Temperature dependences of the magnetic entropies S_{mag} for TmV_2Al_{20} in various magnetic fields along the [100] direction.

6 J/(mol K^2), which is surprisingly large, compared with values for normal metallic compounds. This result suggests that the ground state for TmV_2Al_{20} is a doublet (Γ_3) rather than a singlet (Γ_1, Γ_2).

The magnetic entropy S_{mag} vs T curves in various external fields along the [100] direction were plotted in Figure 6.3(d). The magnetic entropies below 0.5 K were obtained by integrating C_{mag} / T from 0 to 0.5 K, in which the C_{mag} / T values below 0.5 K were estimated by the linear extrapolations of the data below 1.0 K to 0 K. The S_{mag} ($\mu_0 H$ = 0 T) value reaches R ln 5 near 10 K, which implies that a magnetic triplet state locates near above the Γ_3 doublet ground state (pseudo-fivefold ground state). S_{mag} values and their increasing rates with respect to temperature in nonzero field is suppressed with increasing applied fields, taking smaller values.

6.1.3. Electrical resistivity

Figure 6.4(a) shows temperature dependences of electrical resistivities for TmV_2Al_{20} single crystal and polycrystalline LaV_2Al_{20}. The same polycrystalline LaV_2Al_{20} sample as in the previous chapter was used to get the magnetic part of resistivity for TmV_2Al_{20}. The residual resistivity ratios RRR = ρ(300 K)/ρ(2 K) for TmV_2Al_{20} and LaV_2Al_{20} are about 3 and 25, respectively. The resistivity of TmV_2Al_{20} increase rapidly from 2 K with increasing temperature and shows a broad shoulder near 30 K. As shown in Figure 6.4(b), the broad shoulder near 30 K can also be observed in the magnetic part of resistivity ρ_{mag} for TmV_2Al_{20}, ρ_{mag} increases gradually from 30 K to about 90 K, and then increases rapidly with increasing

temperature. This behavior can be attributed to the CEF effect, suggesting an overall CEF splitting of about 90 K.

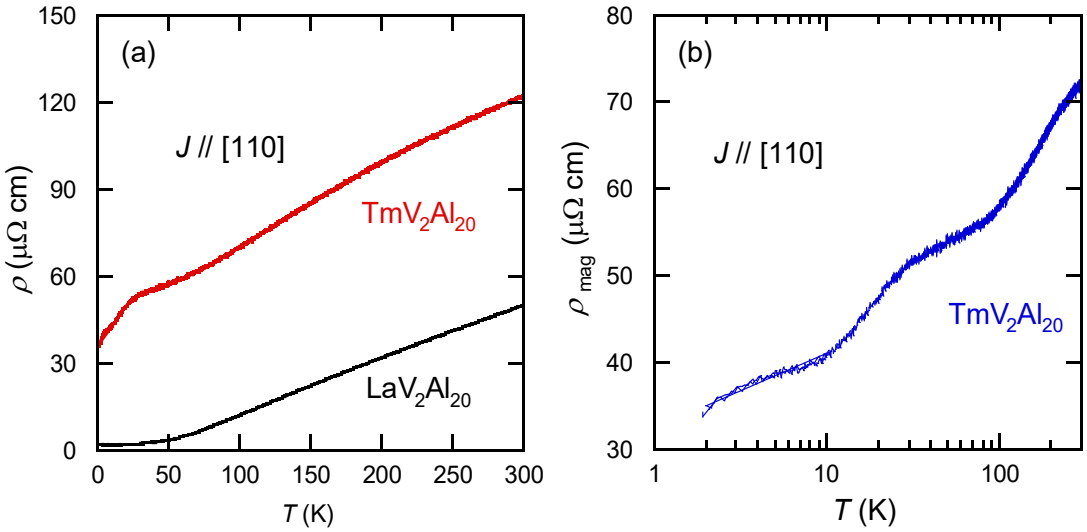

Figure 6.4: (a) Temperature dependences of electrical resistivities for TmV_2Al_{20} single crystal and polycrystalline LaV_2Al_{20}. (b) Magnetic part of electrical resistivity for TmV_2Al_{20} on a logarithmic temperature scale with the current J along the [110] direction in zero field.

6.2. Analyses and discussion

We adopt the following Hamiltonian to analyze the magnetic and thermal properties of TmV_2Al_{20},

$$\mathcal{H} = \mathcal{H}_{\mathrm{CEF}} + \mathcal{H}_{\mathrm{Z}} + \mathcal{H}_{\mathrm{exch}} , \tag{6.1}$$

where $\mathcal{H}_{\mathrm{CEF}}$ is the crystalline-electric-field Hamiltonian, $\mathcal{H}_{\mathrm{Z}}$ is the Zeeman Hamiltonian, and $\mathcal{H}_{\mathrm{exch}}$ is the exchange Hamiltonian between Tm atoms. We treated the exchange interaction in the frame of the molecular-field approximation. $\mathcal{H}_{\mathrm{CEF}}$ is written as

$$\mathcal{H}_{\mathrm{CEF}} = W\left(x\frac{O_4}{F(4)} + (1-|x|)\frac{O_6}{F(6)}\right), \tag{6.2}$$

where $O_4 = O_4^0 + 5O_4^4$ and $O_6 = O_6^0 - 21O_6^4$. $\mathcal{H}_{\mathrm{Z}}$ and $\mathcal{H}_{\mathrm{exch}}$ are expressed as

$$\mathcal{H}_{\mathrm{Z}} = g_J\mu_{\mathrm{B}}\boldsymbol{J}\boldsymbol{H}_{\mathrm{ext}}\,, \tag{6.3}$$

$$\mathcal{H}_{\mathrm{exch}} = g_J\mu_{\mathrm{B}}\boldsymbol{J}\boldsymbol{H}_{\mathrm{mol}}\,, \tag{6.4}$$

where $\boldsymbol{H}_{\mathrm{ext}}$ is the external magnetic field, and $\boldsymbol{H}_{\mathrm{mol}}$ is the molecular field at Tm site caused by the surrounding Tm atoms. $\boldsymbol{H}_{\mathrm{mol}}$ is defined as $n(g_J\mu_{\mathrm{B}})\langle\boldsymbol{J}\rangle$ where n is the exchange coupling parameter between Tm atoms. The physical quantities of $\boldsymbol{J}$, $\boldsymbol{H}_{\mathbf{ext}}$, and $\boldsymbol{H}_{\mathrm{mol}}$ are three-dimensional vectors. The magnetization $\boldsymbol{M}$ is calculated by

$$\boldsymbol{M} = -g_J\mu_{\mathrm{B}}\langle\,\boldsymbol{J}\,\rangle = -g_J\mu_{\mathrm{B}}\frac{\mathrm{Tr}\,\boldsymbol{J}\exp(-\beta\mathcal{H})}{\mathrm{Tr}\exp(-\beta\mathcal{H})}\,, \tag{6.5}$$

where $\langle\,\boldsymbol{J}\,\rangle$ is the thermal average of the total angular momentum and $\beta = 1/k_{\mathrm{B}}\,T$. Equation (6.5) is solved by the iteration method. The specific heat C is calculated by

$$C = N_{\mathrm{A}}\frac{\partial}{\partial T}\left(\langle\mathcal{H}\rangle - \frac{1}{2}\langle\mathcal{H}_{\mathrm{exch}}\rangle\right), \tag{6.6}$$

We have three fitting parameters, i.e., W, x, and n to calculate M (T, H) and C (T, H) using the above Hamiltonian. However, at the beginning, we ignored the effect of exchange interaction by setting $n = 0$ because of the small value of the experimental θ_{p}. First, we tuned the parameters W and x to appropriate values to reproduce the experimental results of M (H,T) and C_{mag} (H, T), considering the pseudo-fivefold degeneracy and the observed magnetic anisotropies. Then, the parameter n was adjusted to fit the experimental results.

In the iteration process, we referred the previous work by Lea *et al*. [104] for the CEF energy scheme of the Tm^{3+} ions in the cubic site symmetry. According to their diagram, the

doublet ground state-triplet first excited state is realized in the regions of $-1 \leq x \leq -0.55$ for the positive W (we name this region as region I) and $0.8 \leq x \leq 1$ for the negative W (region II). The triplet ground state-doublet first excited state is realized in the region $-0.55 \leq x \leq 0.2$ for the positive W (region III). The energy separation between the two lowest energy levels is speculated to be several Kelvin because the entropy reaches R ln 5 at approximately 10 K. Concerning the easy direction of magnetization, the calculations using Equation (6.5) with various W and x values reveal that [100] easy direction is realized in the regions I, II, and in the narrow region near $x = 0.4$ for $W \geq 1$ K. From the iteration of W and x values, we concluded that the most appropriate W and x are 0.5 K and -0.6, respectively. The nonmagnetic ground state was realized when $-0.9 \leq n \leq 0.2$, and the best fit to the experimental results of magnetizations and specific heats was obtained when $n = 0$.

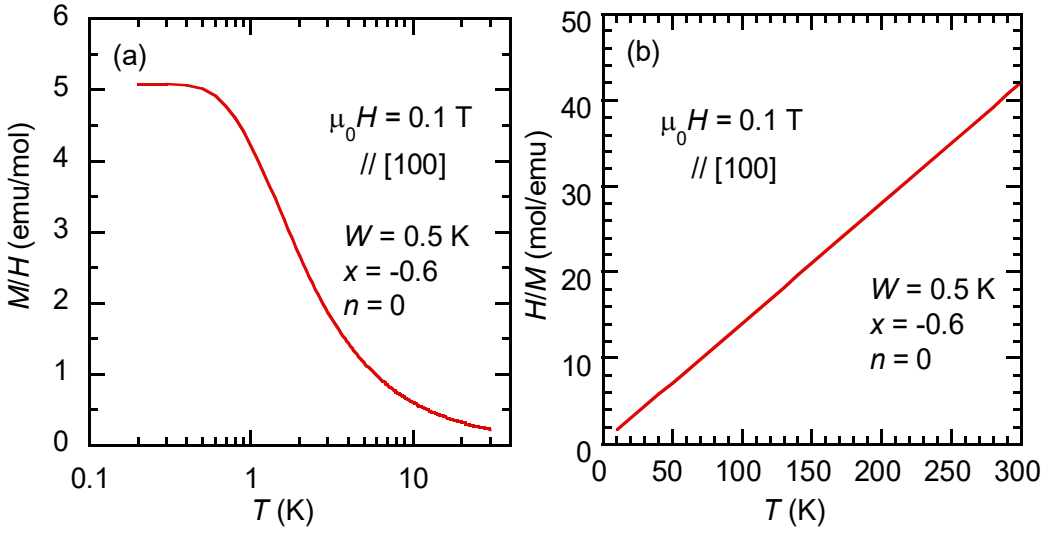

Figure 6.5: (a) Calculated temperature dependence of the susceptibility M / H for TmV_2Al_{20} measured in an applied magnetic field of 0.1 T along [100] axis on a logarithmic temperature scale. (b) Calculated temperature dependence of H / M for TmV_2Al_{20} in a field of 0.1 T along [100] axis.

Figure 6.5(a) shows the calculated temperature dependence of the susceptibility M / H for TmV_2Al_{20} measured in an applied magnetic field of 0.1 T along [100] axis on a logarithmic temperature scale. In the low temperature region below 0.5 K, the susceptibility M/H value tends to saturate, indicating a nonmagnetic doublet ground state. The calculated temperature dependence of H / M for TmV_2Al_{20} in a field of 0.1 T along [100] axis was displayed in Figure 6.5(b).

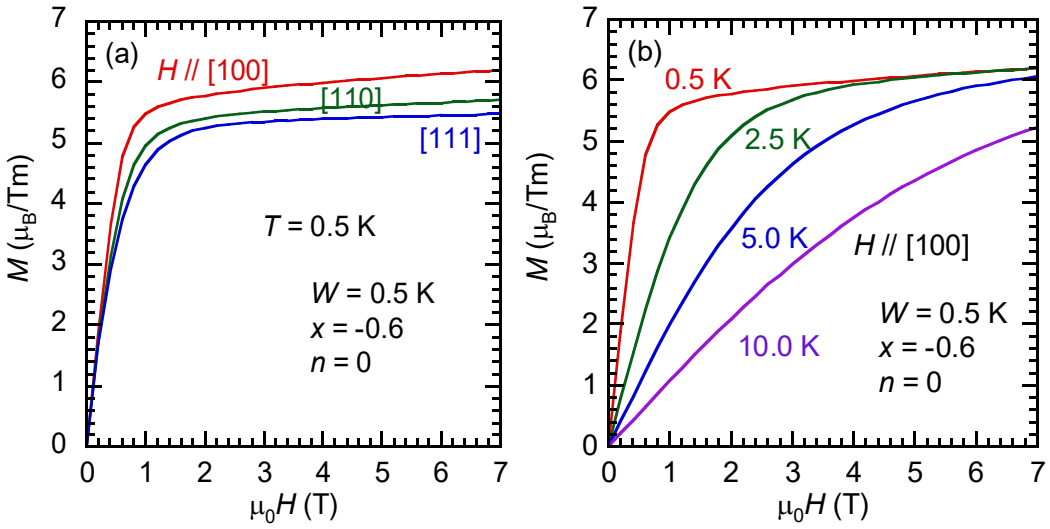

Figure 6.6: Calculated magnetization curves of TmV_2Al_{20} in H (a) along the [100], [110], and [111] directions at 0.5 K, (b) along the [100] direction at various temperatures.

Figure 6.6(a) shows the calculated M (H) curves at 0.5 K in the fields along the [100], [110], and [111] directions. The easy and the hard directions of magnetization are satisfactorily reproduced by the calculations. Figure 6.6(b) shows the calculated M (H) curves at 0.5, 2.5, 5.0, and 10 K in the fields along the [100] direction, in which the profile of experimental curves at each temperature is well reproduced by the calculations. The energy

level scheme derived by using the parameters $W = 0.5$ K, $x = -0.6$, and $n = 0$ is: Γ_3 (0 K, doublet), $\Gamma_5^{(1)}$ (2 K, triplet), Γ_2 (59 K, singlet), $\Gamma_5^{(2)}$ (65 K, triplet), Γ_4 (74 K, triplet) and Γ_1 (85 K, singlet). The ground state Γ_3 is a nonmagnetic doublet, and thus the expectation of $\boldsymbol{J}$ in this state is zero. The magnetization must originate from the mixing between the ground state and the nearby magnetic triplet $\Gamma_5^{(1)}$. This pseudo-fivefold energy level induces the anisotropic magnetizations as shown in Figure 6.6(a). These calculated M values are similar to the experimental ones, thus the reduction of magnetization from the saturation magnetization of free Tm^{3+} ion (7.0 μ_B) is most likely ascribed to the CEF effect.

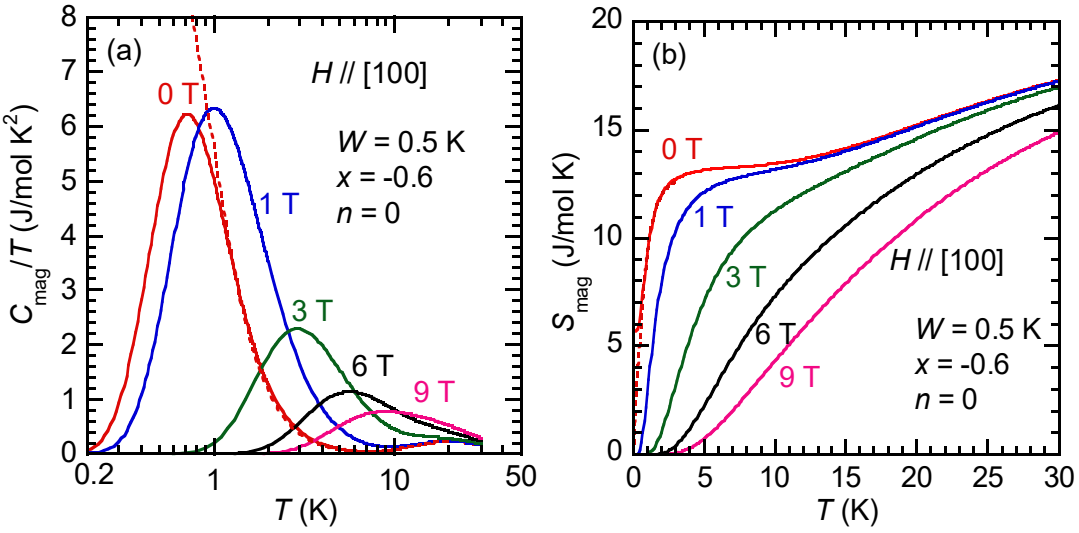

Figure 6.7: (a) Temperature dependences of the calculated C_{mag} / T in various magnetic fields along [100], the dashed line is the C_{mag} / T curve in zero external field considering the splitting of the doublet ground state. (b) Calculated magnetic entropy S_{mag} of TmV_2Al_{20} in various magnetic fields along [100].

Figure 6.7(a) shows the temperature dependences of the calculated C_{mag} / T in the external fields of 0, 1, 3, 6, 9 T along the [100] direction on a logarithmic temperature scale (solid

lines). The calculations reproduced the experimental C_{mag} / T vs T curves when the external fields are nonzero. The calculated C_{mag} / T vs T curve in zero field, however, makes a peak at approximately 0.7 K, which is originated from the small energy gap between the ground state and the first excited state. This behavior of C_{mag} / T contradicts the fact that the experimental C_{mag} / T values increase with decreasing temperature in the lowest temperature region. We tentatively employed a model that Tm^{3+} ions are in a doublet ground state split by small various energy widths y, ranging from 0 to d:

$$E(y) = \frac{ye^{-y\beta} + \varepsilon_3 e^{-\varepsilon_3 \beta} + \cdots}{1 + e^{-y\beta} + e^{-\varepsilon_3 \beta} + \cdots}, \tag{6.7}$$

$$\langle E \rangle = \frac{1}{d} \int_0^d E(y) dy. \tag{6.8}$$

where ε_3, ...are eigen energies above the doublet ground states. Setting d to be 1 K, the specific heat is numerically calculated by $C = d\langle E \rangle / dT$. The dashed line in Figure 6.7 (a) shows the calculation result. The experimental C_{mag} / T vs T curve in zero field in Figure 6.3(b) was reproduced by the calculation.

Figure 6.7(b) shows the temperature dependences of the calculated S_{mag}, of which the values above 0.8 K are quantitatively in good agreement with the experimental ones. The S_{mag} near 10 K in zero field is R ln 5 [13.4 J/(mol K)], corresponding to the pseudo-fivefold degeneracy of the low lying energy levels. In the above model, S_{mag} ($\mu_0 H$ = 0 T) goes to zero at 0 K, as shown by the dashed line in Figure 6.7(b). The mechanism splitting the energy level of the doublet ground state is not clear for the moment, but a small lattice distortion around Tm ions and the quadrupole ordering could result in the energy splitting of the non-

Kramers Γ_3 doublet. Further study is needed to clarify the possible presence of quadrupole ordered state that has been observed in the isostructural Pr-based compounds.

6.3. Conclusion

The magnetization and specific heat of TmV_2Al_{20} single crystals were measured in the temperature range from 0.5 to 300 K in external magnetic fields up to 7 T. TmV_2Al_{20} was found to be paramagnetic above 0.5 K. Clear magnetic anisotropy was observed along the three principal crystallographic axes in the field above 1 T at 0.5 K. The magnetically easy axis is along the [100] direction, and the hard axis is along the [111] direction.

On cooling below 2 K in zero external field, the magnetic part of specific heat divided by temperature, C_{mag} / T, increases up to 6 J/(mol K^2) near 0.6 K. The magnetic entropy in zero field reaches R ln 5 near 10 K, suggesting that the ground state of Tm^{3+} ions is a nonmagnetic doublet state with the first excited state of a magnetic triplet state nearby (a pseudo-fivefold degenerate state).The electrical resistivities for TmV_2Al_{20} single crystal and polycrystalline LaV_2Al_{20} were measured down to 2 K, an overall CEF splitting of about 90 K was suggested by the observed magnetic part of resistivity for TmV_2Al_{20}, which is in good agreement with the proposed CEF scheme.

The experimental results were reproduced by the crystalline electric field calculations, and an energy level scheme was proposed: Γ_3 (0 K, doublet) – $\Gamma_5^{(1)}$ (2 K, triplet) – Γ_2 (59 K, singlet) – $\Gamma_5^{(2)}$ (65 K, triplet) – Γ_4 (74 K, triplet) – Γ_1 (85 K, singlet). The enhanced value of C_{mag} / T in the lowest temperature region in zero field was explained by assuming an energy splitting of the doublet ground state.

References

[1] V. M. T. Thiede, W. Jeitschko, S. Niemann, and T. Ebel, J. Alloys Compd. **267**, 23 (1998).

[2] T. Kuwai, M. Funane, K. Tada, T. Mizushima, and Y. Isikawa, J. Phys. Soc. Jpn. **82**, 074705 (2013).

[3] M. Tsujimoto, Y. Matsumoto, T. Tomita, A. Sakai, and S. Nakatsuji, Phys. Rev. Lett. **113**, 267001 (2014).

[4] T. Tanaka and Y. Kubo, J. Phys. Soc. Jpn. **80**, SA125 (2011).

[5] M. S. Torikachvili, S. Jia, E. D. Mun, S. T. Hannahs, R. C. Black, W. K. Neils, D. Martien, S. L. Bud'ko, and P. C. Canfield, Proc. Natl. Acad. Sci. U. S. A. **104**, 9960 (2007).

[6] Y. Isikawa, J. Ejiri, T. Mizushima, and T. Kuwai, J. Phys. Soc. Jpn. **82**, 123708 (2013).

[7] T. Namiki, K. Nosaka, K. Tsuchida, Q. Lei, R. Kanamori, and K. Nishimura, J. Phys.: Conf. Ser. **683**, 012017 (2016).

[8] V. W. Burnett, D. Yazici, B. D. White, N. R. Dilley, A. J. Friedman, B. Brandom, and M. B. Maple, J. Solid State Chem. **215**, 114 (2014).

[9] Y. Isikawa, T. Mizushima, K. Kumagai, and T. Kuwai, J. Phys. Soc. Jpn. **82**, 83711 (2013).

[10] M. Daszkiewicz, P. Swatek, and D. Kaczorowski, J. Alloys Compd. **517**, 26 (2012).

[11] Y. Muro, K. Motoya, Y. Saiga, and T. Takabatake, J. Phys. Soc. Jpn. **78**, 083707 (2009).

[12] T. Hirose, Y. Okamoto, J. Yamaura, and Z. Hiroi, J. Phys. Soc. Jpn. **84**, 113701 (2015).

[13] M. M. Koza, A. Leithe-Jasper, E. Sischka, W. Schnelle, H. Borrmann, H. Mutka, and Y. Grin, Phys. Chem. Chem. Phys. **16**, 27119 (2014).

[14] D. T. Adroja, a D. Hillier, Y. Muro, T. Takabatake, a M. Strydom, A. Bhattacharyya, A. Daoud-Aladin, and J. W. Taylor, Phys. Scr. **88**, 068505 (2013).

[15] S. Takai, T. Matsumura, H. Tanida, and M. Sera, Phys. Rev. B **92**, 174427 (2015).

[16] T. Takesaka, K. Oe, R. Kobayashi, Y. Kawamura, T. Nishioka, H. Kato, M. Matsumura, and K. Kodama, J. Phys.: Conf. Ser. **200**, 012201 (2010).

[17] T. Mizushima, Y. Watanabe, J. Ejiri, T. Kuwai, and Y. Isikawa, J. Phys.: Conf. Ser. **592**, 012051 (2015).

[18] M. Sakoda, K. Kubota, S. Tanaka, E. Matsuoka, H. Sugawara, T. D. Matsuda, and Y. Haga, J. Phys. Soc. Jpn. **81**, SB011 (2012).

[19] T. Keiber, F. Bridges, R. E. Baumbach, and M. B. Maple, Phys. Rev. B **86**, 174106 (2012).

[20] H. Sato, D. Kikuchi, K. Tanaka, H. Aoki, K. Kuwahara, Y. Aoki, M. Kohgi, H. Sugawara, and K. Iwasa, J. Magn. Magn. Mater. **310**, 188 (2007).

[21] H. Sato, Y. Abe, T. D. Matsuda, K. Abe, T. Namiki, H. Sugawara, and Y. Aoki, J. Magn. Magn. Mater. **258-259**, 67 (2003).

[22] H. Sato, H. Sugawara, D. Kikuchi, S. Sanada, K. Tanaka, H. Aoki, K. Kuwahara, Y. Aoki, and M. Kohgi, Phys. B: Condens. Matter **378-380**, 46 (2006).

[23] H. Sato, Y. Aoki, T. Namiki, T. D. Matsuda, K. Abe, S. Osaki, S. R. Saha, and H. Sugawara, Phys. B: Condens. Matter **328**, 34 (2003).

[24] T. Namiki, C. Sekine, K. Matsuhira, M. Wakeshima, and I. Shirotani, J. Phys. Soc. Jpn. **77**, 336 (2008).

[25] S. Tsutsui, H. Uchiyama, J. P. Sutter, A. Q. R. Baron, J. Yamaura, H. Sugawara, and H. Sato, J. Phys.: Conf. Ser. **391**, 012074 (2012).

[26] M. B. Maple, Z. Henkie, W. M. Yuhasz, P.-C. Ho, T. Yanagisawa, T. a. Sayles, N. P. Butch, J. R. Jeffries, and a. Pietraszko, J. Magn. Magn. Mater. **310**, 182 (2007).

[27] S. Chi, P. Dai, T. Barnes, H. J. Kang, J. W. Lynn, R. Bewley, F. Ye, M. B. Maple, Z. Henkie, and A. Pietraszko, Phys. Rev. B **77**, 094428 (2008).

[28] S. Gupta and K. G. Suresh, J. Alloys Compd. **618**, 562 (2015).

[29] S. Baran, M. Hofmann, J. Leciejewicz, B. Penc, M. Ślaski, and A. Szytuła, J. Alloys Compd. **281**, 92 (1998).

[30] E. Morosan, S. L. Bud'ko, P. C. Canfield, M. S. Torikachvili, and A. H. Lacerda, J. Magn. Magn. Mater. **277**, 298 (2004).

[31] Y. Isikawa, T. Kuwai, T. Mizushima, T. Abe, G. Nakamura, and J. Sakurai, Phys. B: Condens. Matter **281-282**, 365 (2000).

[32] J. Sakurai, D. Huo, D. Kato, T. Kuwai, Y. Isikawa, and K. Mori, Phys. B: Condens. Matter **281-282**, 98 (2000).

[33] S. Hane, T. Goto, T. Abe, and Y. Isikawa, Phys. B: Condens. Matter **281-282**, 391 (2000).

[34] N. Takeda and M. Ishikawa, Phys. B: Condens. Matter **259-261**, 92 (1999).

[35] R. Higashinaka, T. Maruyama, A. Nakama, R. Miyazaki, Y. Aoki, and H. Sato, J. Phys. Soc. Jpn. **80**, 093703 (2011).

[36] A. Sakai and S. Nakatsuji, J. Phys. Soc. Jpn. **80**, 063701 (2011).

[37] K. Matsubayashi, T. Tanaka, J. Suzuki, A. Sakai, S. Nakatsuji, K. Kitagawa, Y. Kubo, and Y. Uwatoko, JPS Conf. Proc. **3**, 011077 (2014).

[38] D. D. Koelling, B. D. Dunlap, and G. W. Crabtree, Phys. Rev. B **31**, 4966 (1985).

[39] T. Takeuchi, S. Yoshiuchi, M. Ohya, Y. Taga, Y. Hirose, K. Sugiyama, F. Honda, M. Hagiwara, K. Kindo, R. Settai, Y. Onuki, and Y. Ōnuki, J. Phys. Soc. Jpn. **80**, 114703 (2011).

[40] H. Sugawara, M. Kobayashi, S. Osaki, S. R. Saha, T. Namiki, Y. Aoki, and H. Sato, Phys. Rev. B **72**, 014519 (2005).

[41] G. R. Stewart, Rev. Mod. Phys. **56**, 755 (1984).

[42] D. K. Singh, A. Thamizhavel, J. W. Lynn, S. Dhar, J. Rodriguez-Rivera, and T. Herman, Sci. Rep. **1**, 1 (2011).

[43] M. Tsubota, S. Tsutsui, D. Kikuchi, H. Sugawara, H. Sato, and Y. Murakami, J. Phys. Soc. Jpn. **77**, 073601 (2008).

[44] M. Okawa, M. Matsunami, K. Ishizaka, R. Eguchi, M. Taguchi, A. Chainani, Y. Takata, M. Yabashi, K. Tamasaku, Y. Nishino, T. Ishikawa, K. Kuga, N. Horie, S. Nakatsuji, and S. Shin, Phys. Rev. Lett. **104**, 247201 (2010).

[45] K. Yoshimura, N. Tsujii, K. Sorada, Takashi Kawabata, H. Mitamura, T. Goto, and K. Kosuge, Phys. B: Condens. Matter **281**, 141 (2000).

[46] A. Yamasaki, S. Imada, H. Higashimichi, H. Fujiwara, T. Saita, T. Miyamachi, A. Sekiyama, H. Sugawara, D. Kikuchi, H. Sato, A. Higashiya, M. Yabashi, K. Tamasaku, D. Miwa, T. Ishikawa, and S. Suga, Phys. Rev. Lett. **98**, 156402 (2007).

[47] W. Higemoto, T. U. Ito, K. Ninomiya, T. Onimaru, K. T. Matsumoto, and T. Takabatake, Phys. Rev. B **85**, 235152 (2012).

[48] T. J. Sato, S. Ibuka, Y. Nambu, T. Yamazaki, T. Hong, A. Sakai, and S. Nakatsuji, Phys. Rev. B **86**, 184419 (2012).

[49] Y. Shimura, M. Tsujimoto, B. Zeng, Q. Zhang, L. Balicas, A. Sakai, and S. Nakatsuji, J. Phys.: Conf. Ser. **683**, 012012 (2016).

[50] F. Honda, S. Yasui, S. Yoshiuchi, T. Takeuchi, R. Settai, and Y. Ōnuki, J. Phys. Soc. Jpn. **79**, 083709 (2010).

[51] S. Paschen and J. Larrea J, J. Phys. Soc. Jpn. **83**, 1 (2014).

[52] Y. Shimura, M. Tsujimoto, B. Zeng, L. Balicas, A. Sakai, and S. Nakatsuji, Phys. Rev. B **91**, 241102 (2015).

[53] A. Sakai, K. Kuga, and S. Nakatsuji, J. Phys. Soc. Jpn. **81**, 083702 (2012).

[54] T. Onimaru, K. T. Matsumoto, Y. F. Inoue, K. Umeo, Y. Saiga, Y. Matsushita, R. Tamura, K. Nishimoto, I. Ishii, T. Suzuki, and T. Takabatake, J. Phys. Soc. Jpn. **79**, 033704 (2010).

[55] S. Niemann and W. Jeitschko, J. Solid State Chem. **114**, 337 (1995).

[56] N. Gross, T. Nasch, and W. Jeitschko, J. Solid State Chem. **293**, 288 (2001).

[57] F. C. Frank and J. S. Kasper, Acta Crystallogr. **11**, 184 (1958).

[58] T. Nasch, W. Jeitschko, and U. C. Rodewald, Z. Naturforsch. B **52**, 1023 (1997).

[59] M. J. Kangas, D. C. Schmitt, A. Sakai, S. Nakatsuji, and J. Y. Chan, J. Solid State Chem. **196**, 274 (2012).

[60] L. J. Treadwell, J. D. McAlpin, D. C. Schmitt, M. J. Kangas, M. T. Sougrati, N. Haldolaarachchige, D. P. Young, J.-C. Jumas, and J. Y. Chan, Inorg. Chem. **52**, 5055 (2013).

[61] M. J. Winiarski, B. Wiendlocha, M. Sternik, P. Wiśniewski, J. R. O'Brien, D. Kaczorowski, and T. Klimczuk, Phys. Rev. B **93**, 134507 (2016).

[62] Y. Matsumoto, T. D. Matsuda, N. Tateiwa, E. Yamamoto, Y. Haga, and Z. Fisk, J.

Korean Phys. Soc. **63**, 363 (2013).

[63] S. Jia, N. Ni, S. Bud'ko, and P. Canfield, Phys. Rev. B **80**, 104403 (2009).

[64] T. Kubo, H. Kotegawa, H. Tou, R. Higashinaka, A. Nakama, Y. Aoki, and H. Sato, J. Phys.: Conf. Ser. **592**, 012093 (2015).

[65] T. Kubo, H. Kotegawa, H. Tou, R. Higashinaka, A. Nakama, Y. Aoki, and H. Sato, JPS Conf. Proc. **3**, 012031 (2014).

[66] A. Sakai and S. Nakatsuji, Phys. Rev. B **84**, 201106 (2011).

[67] Y. Hirose, K. Enoki, S. Yoshiuchi, T. Takeuchi, F. Honda, K. Sugiyama, E. Yamamoto, Y. Haga, M. Hagiwara, K. Kindo, R. Settai, and Y. Ōnuki, J. Phys.: Conf. Ser. **391**, 012021 (2012).

[68] R. Higashinaka, A. Nakama, M. Ando, M. Watanabe, Y. Aoki, and H. Sato, J. Phys.: Conf. Ser. **273**, 012033 (2011).

[69] R. Higashinaka, A. Nakama, M. Ando, M. Watanabe, Y. Aoki, and H. Sato, J. Phys. Soc. Jpn. **80**, SA048 (2011).

[70] T. Onimaru, K. T. Matsumoto, Y. F. Inoue, K. Umeo, T. Sakakibara, Y. Karaki, M. Kubota, and T. Takabatake, Phys. Rev. Lett. **106**, 177001 (2011).

[71] I. Ishii, H. Muneshige, Y. Suetomi, T. K. Fujita, T. Onimaru, K. T. Matsumoto, T. Takabatake, K. Araki, M. Akatsu, Y. Nemoto, T. Goto, and T. Suzuki, J. Phys. Soc. Jpn. **80**, 093601 (2011).

[72] T. Onimaru, N. Nagasawa, K. T. Matsumoto, K. Wakiya, K. Umeo, S. Kittaka, T. Sakakibara, Y. Matsushita, and T. Takabatake, Phys. Rev. B **86**, 184426 (2012).

[73] N. Nagasawa, T. Onimaru, K. T. Matsumoto, K. Umeo, and T. Takabatake, J. Phys.: Conf. Ser. **391**, 012051 (2012).

[74] M. Matsunami, M. Taguchi, A. Chainani, R. Eguchi, M. Oura, A. Sakai, S. Nakatsuji, and S. Shin, Phys. Rev. B **84**, 193101 (2011).

[75] T. Kubo, H. Kotegawa, H. Tou, R. Higashinaka, A. Nakama, Y. Aoki, and H. Sato, J. Phys. Soc. Jpn. **84**, 074701 (2015).

[76] A. Sakai and S. Nakatsuji, J. Phys.: Conf. Ser. **391**, 012058 (2012).

[77] K. Araki, Y. Shimura, N. Kase, T. Sakakibara, A. Sakai, and S. Nakatsuji, JPS Conf. Proc. **3**, 011093 (2014).

[78] Y. Tokunaga, H. Sakai, S. Kambe, A. Sakai, S. Nakatsuji, and H. Harima, Phys. Rev. B **88**, 085124 (2013).

[79] M. Tsujimoto, Y. Matsumoto, and S. Nakatsuji, J. Phys.: Conf. Ser. **592**, 012023 (2015).

[80] Y. Machida, T. Yoshida, T. Ikeura, K. Izawa, A. Nakama, R. Higashinaka, Y. Aoki, H. Sato, A. Sakai, S. Nakatsuji, N. Nagasawa, K. Matsumoto, T. Onimaru, and T. Takabatake, J. Phys.: Conf. Ser. **592**, 012025 (2015).

[81] K. Matsubayashi, T. Tanaka, A. Sakai, S. Nakatsuji, Y. Kubo, and Y. Uwatoko, Phys.

Rev. Lett. **109**, 187004 (2012).

[82] M. Tsujimoto, Y. Matsumoto, T. Tomita, A. Sakai, and S. Nakatsuji, Phys. Rev. Lett. **113**, 267001 (2014).

[83] M. Tsujimoto, A. Sakai, and S. Nakatsuji, JPS Conf. Proc. **3**, 011074 (2014).

[84] Y. Shimura, M. Tsujimoto, A. Sakai, B. Zeng, L. Balicas, and S. Nakatsuji, J. Phys.: Conf. Ser. **592**, 012026 (2015).

[85] R. Higashinaka, A. Yamada, R. Miyazaki, Y. Aoki, M. Mizumaki, S. Tsutsui, K. Nitta, T. Uruga, and H. Sato, JPS Conf. Proc. **3**, 011079 (2014).

[86] Y. Nakanishi, T. Fujino, K. Ito, M. Nakamura, M. Yoshizawa, Y. Saiga, M. Kosaka, and Y. Uwatoko, Phys. Rev. B **80**, 184418 (2009).

[87] T. Takeuchi, S. Yoshiuchi, M. Ohya, Y. Taga, Y. Hirose, K. Sugiyama, F. Honda, M. Hagiwara, K. Kindo, R. Settai, Y. Onuki, and Y. Ōnuki, J. Phys. Soc. Jpn. **80**, 114703 (2011).

[88] E. D. Bauer, C. Wang, V. R. Fanelli, J. M. Lawrence, E. A. Goremychkin, N. R. de Souza, F. Ronning, J. D. Thompson, A. V. Silhanek, V. Vildosola, A. M. Lobos, A. A. Aligia, S. Bobev, and J. L. Sarrao, Phys. Rev. B **78**, 115120 (2008).

[89] P. Swatek, M. Daszkiewicz, and D. Kaczorowski, Phys. Rev. B **85**, 094426 (2012).

[90] N. Kase, Y. Shimura, S. Kittaka, T. Sakakibara, S. Nakatsuji, T. Nakano, N. Takeda, and J. Akimitsu, J. Phys.: Conf. Ser. **592**, 012052 (2015).

[91] T. Yanagisawa, W. M. Yuhasz, P.-C. Ho, M. Brian Maple, H. Watanabe, T. Ueno, Y. Nemoto, and T. Goto, J. Magn. Magn. Mater. **310**, 223 (2007).

[92] P.-C. Ho, W. M. Yuhasz, N. P. Butch, N. A. Frederick, T. A. Sayles, J. R. Jeffries, M. B. Maple, J. B. Betts, A. H. Lacerda, P. Rogl, and G. Giester, Phys. Rev. B **72**, 094410 (2005).

[93] C. Huang, *Rare Earth Coordination Chemistry: Fundamentals and Applications* (John Wiley & Sons, Singapore, 2011).

[94] N. W. Ashcroft and N. D. Mermin, *Solid State Physics* (W. B. Sanders, Philadelphia, 1976).

[95] E. Tereshina, Magnetic and Magnetoelastic Properties of Intermetallic Compounds of F- and D-Elements with High Content of 3d-Metal and Their Hydrides, Charles University, 2009.

[96] W. J. de Haas, J. de Boer, and G. J. van dën Berg, Physica **1**, 1115 (1934).

[97] J. Kondo, Prog. Theor. Phys. **32**, 37 (1964).

[98] Y. Ōnuki, R. Settai, K. Sugiyama, T. Takeuchi, T. C. Kobayashi, Y. Haga, and E. Yamamoto, J. Phys. Soc. Jpn. **73**, 769 (2004).

[99] Y. Ōnuki, R. Settai, F. Honda, T. Takeuchi, N. Tateiwa, T. D. Matsuda, E. Yamamoto, Y. Haga, and H. Harima, Phys. C: Supercond. **469**, 868 (2009).

[100] J. Lawrence, Mod. Phys. Lett. B **22**, 1273 (2008).

[101] K.H.J.Buschow and F.R. De Boer, *Physics of Magnetism and Magnetic Materials* (Kluwer Academic Publishers, New York, 2003).

[102] K. W. H. Stevens, Proc. Phys. Soc. Sect. A **65**, 209 (1952).

[103] M. T. Hutchings, Solid State Phys. **16**, 227 (1964).

[104] K. R. Lea, M. J. M. Leask, and W. P. Wolf, J. Phys. Chem. Solids **23**, 1381 (1962).

[105] Y. Isikawa, K. Mori, Y. Ogiso, K. Oyabe, and K. Sato, J. Phys. Soc. Jpn. **60**, 2514 (1991).

[106] K. Nishimura, W. D. Hutchison, Y. Tajiri, Y. Isikawa, K. Sato, and K. Kindo, Phys. B Phys. Condens. Matter **406**, 2281 (2011).

[107] R. Triboulet and Y. Marfaing, J. Electrochem. Soc. **120**, 1260 (1973).

[108] M. G. Kanatzidis, R. Pöttgen, and W. Jeitschko, Angew. Chem. Int. Ed. Engl. **44**, 6996 (2005).

[109] P. C. Canfield and Z. Fisk, Philos. Mag. Part B **65**, 1117 (1992).

[110] E. M. Benbow and S. E. Latturner, J. Solid State Chem. **179**, 3989 (2006).

[111] X. Ma, P. Chai, B. Chen, E. Lochner, and S. E. Latturner, J. Solid State Chem. **229**, 181 (2015).

[112] M. Stojanovic and S. E. Latturner, J. Solid State Chem. **180**, 907 (2007).

[113] U. Subbarao, S. Sarkar, and S. C. Peter, J. Solid State Chem. **226**, 126 (2015).

[114] A. Onosaka, Y. Okamoto, J. Yamaura, T. Hirose, and Z. Hiroi, J. Phys. Soc. Jpn. **81**, 123702 (2012).

[115] K. Kuwahara, M. Takagi, K. Iwasa, S. Itobe, D. Kikuchi, Y. Aoki, M. Kohgi, H. Sato, and H. Sugawara, Phys. B **403**, 903 (2008).

[116] Y. Isikawa, T. Mizushima, S. Miyamoto, K. Kumagai, M. Nakahara, H. Okuyama, T. Tayama, T. Kuwai, and P. Lejay, J. Korean Phys. Soc. **63**, 644 (2013).

[117] Y. Aoki, T. Namiki, T. D. Matsuda, K. Abe, H. Sugawara, and H. Sato, Phys. Rev. B **65**, 064446 (2002).

List of publications

1. Qiankun Lei, Takahiro Namiki, Yosikazu Isikawa, Katsuhiko Nishimura, and Wayne D. Hutchison, *Magnetic and Thermal Properties of the TmV_2Al_{20} Single Crystals*, J. Phys. Soc. Jpn., 2016; **85**: 034709, 5pp.

2. Takahiro Namiki, Qiankun Lei, Yosikazu Isikawa, and Katsuhiko Nishimura, *Possible Heavy Fermion State of the Caged Cubic Compound NdV_2Al_{20}*, J. Phys. Soc. Jpn., 2016; **85**: 073706, 4pp.

3. Takahiro Namiki, Kenta Nosaka, Kyousuke Tsuchida, Qiankun Lei, Ryousuke Kanamori, and Katsuhiko Nishimura, *Magnetic and thermal properties of NdT_2Al_{20} (T: Ti, V, Cr) single crystals*, J. Phys.: Conf. Ser., 2016; **683**: 012017, 4pp.

4. Katsuhiko Nishimura, Kenji Matsuda, Qiankun Lei, Takahiro Namiki, Seungwon Lee, Norio Nunomra, Teiichiro Matsuzaki, and Wayne D. Hutchison, *Early Stage Clustering Behavior in Al-Mg-Si Alloys Observed via Time Dependent Magnetization*, Mater. Trans., 2016; **57**: 627-630.

5. Kelei Zhang, Ruijie Zhao, Qiankun Lei, and Yanchun Hu, *Effect of Calcination Temperature on the Photocatalytic Activity of Spiel Zn_2SnO_4*, Advanced Materials Research, 2012; **476**: 1882-1888.

6. Guang Sun, Chunxin Liu, Qiankun Lei, Jiajia You, and Xiaojun Dai, *Preparation and Optical Properties of Bi_2WO_6 Hollow Nanospheres*, Journal of Henan University of Science & Technology (Natural Science) 2010; **31**: 9-11.

List of tables

Table 2.1: The electron configurations and atomic radiuses of the rare earth elements. [93] 10

Table 2.2: Ground-state properties of the trivalent rare earth ions. [95] 11

List of figures

Figure 1.1: Crystal structure of RT_2X_{20}. R (8a) and T (16d) atoms each occupy their single unique sites with cubic (T_d) and trigonal ($3m$) point symmetry respectively, and X atoms have three different sites, i.e., 16c, 48f, and 96g for X(1) , X(2) , and X(3) , respectively. [65] 2

Figure 2.1: Radial wave functions of 4f, 5s, 5p, 5d, 6s, and 6p electrons for Ce. The radius unit is the atomic unit a_0 = 0.529 Å. [93] 9

Figure 2.2: Doniach's phase diagram. [98] 16

Figure 2.3: Energy schemes of Nd^{3+} ion when W = 1 K. 21

Figure 2.4: Energy schemes of Tm^{3+} ion when W = 1 K. 21

Figure 3.1: Temperature profile for the growth of single crystals from Al flux. 24

Figure 3.2: Single crystals of TmV_2Al_{20} with the typical shape and dimensions. 25

Figure 3.3: XRD patterns of RT_2Al_{20} (R = La, Nd, Tm, Lu, T =Ti, V)..... 26

Figure 3.4: Lattice parameters of RT_2Al_{20} (R = rare earth, T = Ti, V)..... 27

Figure 3.5: The Laue pattern of NdV_2Al_{20} single crystal with the [100] direction perpendicular to the film is shown on the left-hand side, and the calculated Laue pattern is shown on the right-hand side. 28

Figure 4.1: Temperature dependences of (a) the magnetic susceptibility M / H on a logarithmic temperature scale, and (b) the inverse magnetic susceptibility H / M in an applied field of 0.1T along the [110] direction for $NdTi_2Al_{20}$. 31

Figure 4.2: Field dependences of magnetization along the three principal crystallographic axes [100], [110], and [111] at T = 0.5 K in applied fields (a) up to 7 T, (b) from 0 to 0.3 T for $NdTi_2Al_{20}$. Field dependences of magnetization at various temperatures in applied magnetic fields along [110] (c) up to 7 T, and (d) from 0 to 0.5 T for $NdTi_2Al_{20}$. 32

Figure 4.3: Temperature dependences of (a) specific heat C in applied fields of 0, 1, 3, 6, and 9 T on a logarithmic temperature scale, (b) specific heat C for single crystal of $NdTi_2Al_{20}$ in small applied fields below 1 T on a linear temperature scale, (c) specific heat divided by temperature C / T, and (d) magnetic specific heat divided by temperature C_{mag} / T in applied fields of 0, 1, 3, 6, and 9 T on a logarithmic temperature scale for single crystal of $NdTi_2Al_{20}$. The applied fields are along the [110] direction, and the dashed lines denote the specific heat of the nonmagnetic reference compound $LaTi_2Al_{20}$ in zero field. 34

Figure 4.4: Magnetic phase diagram for single crystal of $NdTi_2Al_{20}$ in applied fields along the [110] direction. 35

Figure 4.5: Temperature dependences of the magnetic entropy S_{mag} for $NdTi_2Al_{20}$ in various applied magnetic fields along the [110] direction. 36

Figure 4.6: Temperature dependences of (a) electrical resistivities for $NdTi_2Al_{20}$ and $LaTi_2Al_{20}$ single crystals, (b) magnetic part of electrical resistivity for $NdTi_2Al_{20}$ with the current J along the [110] direction in zero field. 37

Figure 4.7: Calculated temperature dependences of (a) the magnetic susceptibility M / H on a logarithmic temperature scale, and (b) the inverse magnetic susceptibility H / M for $NdTi_2Al_{20}$ in an applied field of 0.1T along the [110] direction. 40

Figure 4.8: Calculated field dependences of magnetization at various constant temperatures (a) in applied magnetic fields along [110] up to 7 T, and (b) below 0.5 T. 41

Figure 4.9: Calculated temperature dependences of (a) the magnetic specific heat in the form of C_{mag} / T, and (b) magnetic entropy S_{mag} for $NdTi_2Al_{20}$ in various applied magnetic fields along the [110] direction. 42

Figure 5.1: (a) Temperature dependences of magnetization M of NdV_2Al_{20} in an applied magnetic field of 0.1 T along the three principal axes and in a field of 0.01 T along the [100] direction. (b) The temperature dependence of the inverse magnetic susceptibility H / M in a field of 0.1 T along the [100] direction. 46

Figure 5.2: (a) Magnetization curves of NdV_2Al_{20} in magnetic fields along the [100] direction. (b) Magnetization curves of NdV_2Al_{20} in magnetic fields along the three principal crystallographic axes at 0.5 K. (c) Magnetization curves below 0.4 T. 47

Figure 5.3: (a) Temperature dependences of the specific heat C for NdV_2Al_{20} in various fields along the [100] direction. The dashed line is the temperature dependence of C for LaV_2Al_{20}. (b) The temperature dependences of the specific heat divided by temperature C / T for NdV_2Al_{20} and LaV_2Al_{20}. 49

Figure 5.4: Temperature dependences of the magnetic part of the entropy S_{mag} for NdV_2Al_{20} in various fields along the [100] direction. 50

Figure 5.5: (a) Temperature dependences of electrical resistivity ρ for single crystals of NdV_2Al_{20} and polycrystalline LaV_2Al_{20} with the current J along the [110] direction in zero field. (b) The temperature dependence of electrical resistivity ρ for NdV_2Al_{20} on a logarithmic temperature scale. 51

Figure 5.6: Calculated magnetizations of Nd^{3+} ion in a cubic symmetry site as functions of the CEF parameters W and x, when (a) $W > 0, -1 \leq x \leq 1$, (b) $W < 0, -1 \leq x \leq 1$. The calculated magnetizations are independent of W. The regions of the x parameter with larger magnetizations (solid lines), are selected. 53

Figure 6.1: (a) Temperature dependence of the susceptibility M / H for TmV_2Al_{20} measured in an applied magnetic field of 0.1 T along [100] axis on a logarithmic temperature scale. (b) Temperature dependence of the inverse susceptibility H / M for TmV_2Al_{20} in a field of 0.1 T along [100] axis, the solid line represents the Curie-Weiss fitting between 50 and 300 K. 56

Figure 6.2: Magnetization curves of TmV_2Al_{20} in the magnetic field up to 7 T (a) along the principal crystallographic axes [100], [110] and [111] at 0.5 K, (b) along the [100] direction at various temperatures. 57

Figure 6.3: (a) Temperature dependences of the specific heat C for TmV_2Al_{20} at various H along the [100] direction, the dashed line is the temperature dependence of the specific heat for LuV_2Al_{20}. Temperature dependences of C_{mag} / T for TmV_2Al_{20} in various magnetic fields along the [100] direction (b) on a logarithmic temperature scale, and (c) on a linear temperature scale, the solid line is a linear extrapolation of the data between 0.5 and 1.0 K to 0 K. (d) Temperature dependences of the magnetic entropies S_{mag} for TmV_2Al_{20} in various magnetic fields along the [100] direction. 59

Figure 6.4: (a) Temperature dependences of electrical resistivities for TmV_2Al_{20} single crystal and polycrystalline LaV_2Al_{20}. (b) Magnetic part of electrical resistivity for TmV_2Al_{20} on a logarithmic temperature scale with the current J along the [110] direction in zero field. 61

Figure 6.5: (a) Calculated temperature dependence of the susceptibility M / H for TmV_2Al_{20} measured in an applied magnetic field of 0.1 T along [100] axis on a logarithmic temperature scale. (b) Calculated temperature dependence of H / M for TmV_2Al_{20} in a field of 0.1 T along [100] axis. 63

Figure 6.6: Calculated magnetization curves of TmV_2Al_{20} in H (a) along the [100], [110], and [111] directions at 0.5 K, (b) along the [100] direction at various temperatures. 64

Figure 6.7: (a) Temperature dependences of the calculated C_{mag} / T in various magnetic fields along [100], the dashed line is the C_{mag} / T curve in zero external field considering the splitting of the doublet ground state. (b) Calculated magnetic entropy S_{mag} of TmV_2Al_{20} in various magnetic fields along [100]. 65

Acknowledgements

First of all, I would like to express my sincere gratitude to my supervisor Professor Katsuhiko Nishimura who gave me the chance to further my study in Japan, for his continuous support, for his cares and concerns in both my life and study, for the time, patience and helpful guidance he has devoted to me.

I would like to acknowledge Associate Professor Takahiro Namiki for his great help in magnetization, specific heat, and electrical resistivity measurements, and for his guidance in experimental techniques and data analyses. My greatest thanks also goes to Emeritus Professor Yosikazu Isikawa in the Department of Physics, for his expertise in magnetism and physics, for useful discussions, and for his great help in theoretical calculations. I would like to thank Professor Tomohiko Kuwai, Associate Professor Toshio Mizushima in the Department of Physics as well as the students in their laboratory, who kindly offered me help and facilities for sample cutting. And I thank all the students in our laboratory during the past three years, who have helped me a lot in experiments and daily life.

I would also like to thank Dr. Wayne D. Hutchison from University of New South Wales in Australia, who visited our laboratory regularly every year, for his helpful suggestions for my research. My special thanks also go to Emeritus Professor Katsunori Mori who introduces me Japanese culture and plays table tennis with me every Thursday after his lecture. I would

like to take the chance to thank all the teachers and friends during my study in University of Toyama.

Last but not the least, I would like to thank my family in China for their love and support during my study in Japan.